Self-consistent modelling of Mercury's exosphere by sputtering, micro-meteorite impact and photon-stimulated desorption

P. Wurz [a,*], J.A. Whitby [a,1], U. Rohner [a,2], J.A. Martín-Fernández [b], H. Lammer [c], C. Kolb [c,3]

[a] Physikalisches Institut, Universität Bern, Sidlerstrasse 5, CH-3012 Bern, Switzerland
[b] Department for Computer Science and Applied Mathematics, University of Girona, Edifici P-IV, Campus Montilivi, E-17071 Girona, Spain
[c] Space Research Institute, Austrian Academy of Sciences, Schmiedlstrasse 6, A-8042 Graz, Austria

ARTICLE INFO

ABSTRACT

A Monte-Carlo model of exospheres (Wurz and Lammer, 2003) was extended by treating the ion-induced sputtering process, photon-stimulated desorption, and micro-meteorite impact vaporisation quantitatively in a self-consistent way starting with the actual release of particles from the mineral surface of Mercury. Based on available literature data we established a global model for the surface mineralogy of Mercury and from that derived the average elemental composition of the surface. This model serves as a tool to estimate densities of species in the exosphere depending on the release mechanism and the associated physical parameters quantitatively describing the particle release from the surface.

Our calculation shows that the total contribution to the exospheric density at the Hermean surface by solar wind sputtering is about $4 \times 10^7 \, \mathrm{m}^{-3}$, which is much less than the experimental upper limit of the exospheric density of $10^{12} \, \mathrm{m}^{-3}$. The total calculated exospheric density from micro-meteorite impact vaporisation is about $1.6 \times 10^8 \, \mathrm{m}^{-3}$, also much less than the observed value. We conclude that solar wind sputtering and micro-meteorite impact vaporisation contribute only a small fraction of Mercury's exosphere, at least close to the surface. Because of the considerably larger scale height of atoms released via sputtering into the exosphere, sputtered atoms start to dominate the exosphere at altitudes exceeding around 1000 km, with the exception of some light and abundant species released thermally, e.g. H_2 and He. Because of Mercury's strong gravitational field not all particles released by sputtering and micro-meteorite impact escape. Over extended time scales this will lead to an alteration of the surface composition.

© 2010 Elsevier Ltd. All rights reserved.

1. Introduction

Observations on board of Mariner 10 with the UV spectrograph established the presence of H, He, and O in Mercury's exosphere (Broadfoot et al., 1976; Shemansky, 1988); ground based observations established the presence of Na, K, and Ca in Mercury's exosphere (e.g., Potter and Morgan, 1985, 1986; Bida et al., 2000; see also Killen et al., 2007 and references therein). MESSENGER observed during the first flyby the tailward distributions of exospheric Na and Ca (McClintock et al., 2008a) and during the second flyby Na, Ca, and Mg (McClintock et al., 2009). A comprehensive discussion of the Mariner 10 measurements is given by Hunten et al. (1988) and has recently been reviewed by Killen et al. (2007). Densities at the sub-solar point were estimated to be 6×10^9 atoms m^{-3} for He and 2.3×10^8 atoms m^{-3} for the thermal component of atomic hydrogen. A supra-thermal component of hydrogen was observed near the limb above the sub-solar point, providing a total number density of $2.3 \times 10^7 \, \mathrm{m}^{-3}$ at the surface. Atomic oxygen was detected in the third Mariner 10 flyby at a level of $4.4 \times 10^{10} \, \mathrm{m}^{-3}$ (Shemansky, 1988), which gives a column density of about $10^{15} \, \mathrm{m}^{-2}$ dependent on the assumed scale height. The observed Na column densities vary over the range from 10^{14}–$10^{16} \, \mathrm{m}^{-2}$ depending upon several factors as reviewed by Killen et al. (2007). The observed Ca densities are in the range $(0.5$–$1.8) \times 10^{12} \, \mathrm{m}^{-3}$ (Bida et al. 2000; Killen et al., 2005).

From observations of the Na content within the exosphere column densities in the range of $(0.15$–$8.6) \times 10^{11}$ at/cm^2 were reported (see review by Killen et al., 2007). These observations revealed spatial and temporal variations of the observed corona (Potter and Morgan, 1985, 1986, 1990, 1997; Killen et al., 1990; Potter et al., 1999; Leblanc et al., 2009), which have been

interpreted as evidence of energetic magnetospheric plasma processes (Potter and Morgan, 1990), or local surface concentration enhancements (Sprague et al., 1997), or due to transport processes from the dayside to the nightside and subsequent reimplantation preferred at high latitudes on the nightside (Leblanc et al., 2003). However, Potter et al. (2007) argue that in the earlier work the derivation of the column densities did not take into account properly the complicated physics of excitation of the Na D line. A large part of the strong variability seen in the optical observations can be explained by Mercury's eccentric orbit and the changing Doppler shift and radiation pressure; the remaining variability in the actual Na particle density is only within a factor three. In the improved analysis the column densities is typically in the range $(3–10) \times 10^{10}$ at/cm^2 over Mercury's year, with extreme values of 2×10^{10} and 11.5×10^{10} at/cm^2 (Potter et al., 2007). This moderate variability in the Na column density was also reported by Kameda et al. (2007) who observed disk-averaged column densities of $(0.94–1.55) \times 10^{11}$ at/cm^2, with larger localised variations. Kameda et al. (2009) searched for correlations of the Na column density data from Potter et al. (2007) with the true anomaly of Mercury, with radial distance, and solar activity, with solar UV irradiation and did not find a statistically significant correlation. Most recently Mura et al. (2009) interpreted the Na distribution observed during Mercury's transit before the Sun on 7 May 2003 (Schleicher et al., 2004) as a combination of solar wind proton precipitation, which is responsible for the chemical alteration of Mercury's surface by freeing Na atoms from its bounds in the minerals, and the subsequent photon-stimulated and thermal desorption. Furthermore, Sprague et al. (1997) suggested that some variations might be related to radar bright terrains. In summary, the observations of a variable Na corona are the result of various surface release processes (e.g., Lammer et al., 2003; Milillo et al., 2005 and references therein; Killen et al., 2007 and references therein):

- solar wind induced ion sputtering at high latitudes,
- photon-stimulated desorption (PSD),
- micro-meteorite impact vaporisation (MIV),
- chemical sources at low latitudes.

The K column densities are lower, in the range 10^{12}–5.4×10^{13} m^{-2} (Potter et al., 2002; Killen et al., 2007), and are as variable as the Na densities. Interestingly, the Na/K ratio in Mercury's exosphere ranges between 30 and 140, which is larger than for most solar system objects where this ratio is around 10 (Potter et al., 2002; Killen et al., 2007). Na and K most likely are released from the surface via PSD, but sputtering and MIV have been considered as well and may even work in concert with PSD.

Mercury has a sufficiently strong magnetic field to create its own magnetosphere to hold off the solar wind from reaching the planet's surface most of the time (e.g., Siscoe and Christopher, 1975; Slavin and Holzer, 1979). Computer modelling of Mercury's magnetosphere has allowed more detailed investigations and it has become clear that large fractions of the magnetosphere are open around the cusps where solar wind ions can access the surface. The size and exact location of these open areas depend on the solar wind plasma parameters, principally the speed, the density, and the magnetic field (Kabin et al., 2000; Sarantos et al., 2001; Kallio and Janhunen, 2003; Massetti et al., 2003; Mura et al., 2005). These calculations predict an integrated ion flux onto Mercury's surface in the range of 1.1×10^{25}–3×10^{26} s^{-1} depending on solar wind plasma parameters and the interplanetary magnetic field. Most of the ion precipitation is within $\pm 60°$ from the sub-solar point at latitudes between $40°$ and $60°$. In addition, there is a narrow band of magnetospheric ions precipitating onto

the surface all around the planet at mid-latitudes, the so-called auroral precipitation (Delcourt et al., 2003; Kallio and Janhunen, 2003; Massetti et al., 2003), where the proton fluxes are of the order of 10^{11} m^{-2} s^{-1} (Kallio and Janhunen, 2003). Ionised exospheric atoms become part of Mercury's magnetosphere and some of them return to the surface and impact at the auroral precipitation bands. For Na ions this flux is calculated to range between 10^8 and 10^9 m^{-2} s^{-1} (Leblanc et al., 2003).

There is considerable evidence that solar wind and to a lesser extent magnetospheric plasma precipitation play a significant role in the formation of the exosphere via ion implantation, sputtering of surface material (e.g. Potter and Morgan, 1990; Wurz and Lammer, 2003; Killen et al., 2007), and chemical alteration (Potter, 1995; Mura et al., 2009). It is assumed that Ca is released into Mercury's exosphere by ion sputtering, the solar wind ions having reached the surface through the cusps at mid-latitudes (Bida et al., 2000; Killen et al., 2005). The reasons for this assumption are (i) the large optical line-width of the Ca line corresponding to a temperature of about 12,000 K or a mean energy of about 2.1 eV and (ii) the proximity of the observed exospheric Ca population to the polar areas where solar wind penetration can occur (Bida et al., 2000). For Ca an exospheric column density of $(1—1.5) \times 10^{12}$ m^{-2} was observed (Bida et al., 2000). Later, Killen et al. (2005) gave a temperature range of 12,000–20,000 K for the exospheric Ca, and proposed that impact vaporisation of CaO and subsequent photo-dissociation could explain the observed Ca exospheric densities as well. Since Ca is likely sputtered from Mercury's surface by the solar wind other surface elements should also be released via sputtering into the exosphere. During the Mercury flyby of MESSENGER on 14 January 2008 the plasma ion spectrometer, FIPS, detected a range of pick-up ions (Zurbuchen et al., 2008); although the mass resolution of FIPS allows only for the identification of mass groups (Na$^+$/Mg$^+$, S$^+$/O$_2^+$, K$^+$/Ca$^+$, and others) the origin of these ions in the refractory material of the surface is clear. Optical measurements by the MASCS instrument during MESSENGER's second flyby (McClintock et al., 2009) have confirmed the presence of energetic magnesium atoms in the exosphere of Mercury, albeit with a different spatial distribution than calcium.

The total pressure at the surface of Mercury is at most 10^{-10} mbar, derived from the upper limit of the density of 10^{12} m^{-3} from by the Mariner 10 occultation experiment (Fjeldbo et al., 1976; Hunten et al., 1988). The exospheric species observed to date (H, He, O, Na, K, and Ca) together give a surface pressure of the exosphere of about 10^{-12} mbar, which is almost two orders of magnitude less than the upper limit of the exospheric pressure of 10^{-10} mbar. Thus, the observed species represent only a small fraction of Mercury's exosphere. Most likely, volatile material is the unobserved remainder of the exosphere as has been conjectured in Killen and Ip (1999), Wurz and Lammer (2003), and Killen et al. (2007).

In the absence of a landing spacecraft to investigate Mercury's surface composition directly there is great interest in a study of the exospheric composition using mass spectrometers in Mercury orbit, since exospheric particles originate directly from the surface. The measurement of exospheric species is also a way in which we can learn more about the planet's surface composition and the processes that release surface material into the exosphere. In preparation for the SERENA investigation (Orsini et al., 2010) to be performed on board of ESA's BepiColombo planetary orbiter (Milillo et al., 2010) we have extended our original Monte-Carlo model which was applied to Mercury's exosphere (Wurz and Lammer, 2003) by treating the ion-induced sputtering, PSD, and MIV source processes from the surface in a self-consistent way. This extended model serves as a tool to quantitatively predict exospheric densities for several release processes using

the actual physical parameters of the release process. We recently completed a similar investigation for the lunar surface and the details of these calculations can be found in Wurz et al. (2007). Many models of Mercury's exosphere have been presented in the literature, but the majority of these models are mostly concerned with the Na exosphere (e.g. Smyth and Marconi, 1995; Leblanc et al., 2003; Mura et al., 2009). Although Na is a very well observed species in Mercury's exosphere it is only a minor constituent.

In Section 2 we have compiled the presently available information on the mineralogical composition of Mercury's surface to formulate a mineralogical model that serves as a basis for the calculations. In Section 3 we establish our mineralogical model from which we derive the elemental composition of the surface by applying a classical linear correlation method (additive method) and as an alternative estimate a compositional data analysis approach based on the method of Aitchison (1986). The derived surface compositions are used in Section 4 for the calculation of the exospheric densities in a self-consistent way. In the present investigation we focus on particle sputtering by the interaction of energetic ions with Mercury's surface because particle sputtering introduces surface material in an approximately stoichiometric way into the exosphere. The turn-over time for the top 1 cm of regolith was estimated to be 1.5×10^5 years (Killen et al., 2007) and it takes several weeks until a monolayer of material is sputtered from a grain, which is when the steady-state composition of the flux of sputtered atoms will reflect the average bulk composition (Betz and Wehner, 1983). The sputter agents used in our study are solar wind ions and magnetospheric ions, with significant lower precipitation fluxes of the magnetospheric ions. In Section 5 we present the calculations of the exospheric densities for sputtering, micro-meteorite impact, and photon stimulated desorption. Sample results for typical conditions of particle release are given, but presenting results the whole possible parameter range for each release process would need much more space. Based on these exospheric densities and the escape of exospheric particles we discuss in Section 6 the induced composition changes of the surface.

2. Mineralogical composition of Mercury's surface

The present knowledge of the mineralogical composition of Mercury's surface has been discussed in several papers in the past, e.g. the most recent review is given by Sprague et al. (2007, and references therein). There are no direct measurements of Mercury's surface composition by the Mariner 10 mission. However, from the first MESSENGER flyby there are disk-averaged spectra available as well as some spatially resolved observations from the MASCS instrument (McClintock et al., 2008b). Most of what we know about the mineralogical composition of Mercury's surface has been derived from ground-based observations in the visible and infrared spectral regions. Earlier observations were integrated disk measurements. Around the year 2000 disk resolved measurements also became available (e.g. Warell et al., 2006; Sprague et al., 2009), but the spatial resolution is limited to 200–300 km because of atmospheric disturbance (Sprague et al., 2007, 2009).

Thus, the results from the ground-based observations have to be interpreted as global averages or at least as averages over a large area on the surface involving several geological units. Where spatially resolved measurements are available (ground- and space-based) they indicate compositional heterogeneity of the surface on the investigated scales (e.g. McClintock et al., 2008b; Sprague et al., 2009; Denevi et al., 2009). Our mineralogical model of Mercury's surface, which is introduced below, can only be seen as a global average. This is not a severe limitation for the present study, since the planned measurements of the exospheric composition by a mass spectrometer in orbit are by their nature averages over large areas (> 400 km) on the surface.

Ground-based measurements of Mercury's surface mineralogy are difficult because of absorption features of the terrestrial atmosphere in the infrared wavelength range, because of seeing, and the planet's closeness to the Sun. In addition, Mercury's surface has experienced space weathering for more than 4 billion years (e.g., Hapke, 2001) and a substantial regolith layer has developed. An additional complication for infrared spectroscopy of the surface arises from the expected large fraction of agglutinates in Mercury's regolith (Langevin, 1997). The small grain size of the regolith grains complicates the spectroscopic identification of minerals on the surface. From laboratory studies it is known that grain sizes of about 30 μm best fit with the observed spectra (Warell and Blewett, 2004). Despite 40 years of infrared spectroscopic observations only a few facts about the surface mineralogy of Mercury are well established, which we will summarise below; recently, Sprague et al. (2007) gave a very detailed review on this topic. Note that infrared spectroscopy probes only the current surface of Mercury, and mostly the top surface of regolith grains. However, the exospheric material originates from this same top surface. To infer the composition of the crust from the modern surface composition involves significant additional work, which is beyond the scope of this paper paper and will be investigated in future studies. Rothery et al. (2010), for example, show how this could be accomplished by combining many different observations that will become available from the BepiColombo mission.

2.1. The presently known mineralogical composition of Mercury's surface

FeO: Blewett et al. (1997) find that FeO with a content of about 3 wt% gave their best fit to the spectra, while Warell and Blewett (2004) compared laboratory spectra with new available Mercury spectra data and found best agreements for a FeO abundance of about 1.2 wt%. Recent MESSENGER observations find that the ferrous oxide content in average surface material is low, less than 2–3 wt% (McClintock et al., 2008b).

TiO$_2$: Blewett et al. (1997) find that a TiO$_2$ content of about 1 wt% yields the best fits with their spectra. Based on the transparency of microwaves in Mercury's regolith a low TiO$_2$ abundance relative to the Moon was also suggested by Mitchell and de Pater (1994). Finally, Warell and Blewett (2004) compared laboratory spectra with new Mercury spectra and found the best agreement for TiO$_2$ at about 0 wt%. Sprague et al. (2009) however reported an upper limit for rutile (TiO$_2$) up to 37% in a radar bright area, dependent on model assumptions. Denevi et al. (2009) suggest that ilmenite concentrations of up to 40% would be consistent with the optical spectral characteristics of 'low-reflectance material' and up to 15% would be consistent with optical and neutron spectrometer results for 'intermediate terrain'.

SiO$_2$: the SiO$_2$ content is expected to lie in the range between 49 wt% and 55 wt% and has been observed in mid-infrared spectra (Sprague et al., 1994).

(Metallic) iron: Hapke (2001) estimated a submicroscopic iron content of about 0.5 wt% in Mercury's regolith, which is similar to the Moon. Blewett et al. (2002) concluded that Mercury's reoglith has very little nano-phase iron. By using an improved analysis Warell (2003) concluded that metallic iron is less than 0.3%. Also, because of the high transparency to microwaves of Mercury

compared to the Moon it was concluded that the elemental iron content cannot be very large (Mitchell and de Pater, 1994). In addition, a value of 0.1 wt% was reported by Warell and Blewett (2004) and Warell et al. (2006). From recent MESSENGER observations a limit for nano-phase iron (npFe[0]) of 0.1–0.2 wt% was derived (McClintock et al., 2008b). Sprague et al. (2009) conclude that Mercury's regolith contains less nano-phase iron and that the nano-phase iron particles are larger in size than is the case for the lunar regolith.

Feldspars: emission features of feldspar have also been identified in mid-infrared spectra of Mercury (Emery et al., 1998). A mixture of feldspars and pyroxenes was proposed by Warell and Blewett (2004) based on comparisons of laboratory spectroscopic data and Mercury spectra. Further, a feldspatic glass-rich surface was also proposed by Warell et al. (2006). However, the available spectral information could also be interpreted in terms of signatures originating from the glassy soil on Mercury's surface that is expected to be very mature after aeons of meteoritic bombardment (Hapke, 2001; Sprague et al., 2007). Recently, Sprague et al. (2009) conclude that at the investigated locations there are 14–28% Na- and K-bearing feldspars at the surface.

Pyroxene: a mixture of feldspars and pyroxenes was suggested by Warell and Blewett (2004) and heterogenously distributed low-iron pyroxene silicates by Warell et al. (2006). The observation of magnesium in the exosphere (McClintock et al., 2009) requires a source of magnesium such as magnesium pyroxene or magnesium-rich olivine (Denevi et al., 2009).

Olivine: Emery et al. (1998) suggested the presence of olivine by analysing emission features in mid-infrared spectra of Mercury. Olivine is likely present, but close to the Mg-rich end-member because little FeO is observed (Sprague et al., 1994, 2007).

Ca-rich minerals: Warell et al. (2006) attributed the shapes and widths of two near polar near-IR spectra to the presence of Ca-rich clinopyroxene. These results are in line with findings from mid-IR spectral studies presented by Sprague et al. (2002) who obtained Mercury emissivity spectra similar to those of Ca-rich diopside reference laboratory spectra. These findings are also in agreement with recent spectral emissivity measurements of Mercury's surface by Sprague et al. (2009) that indicate Ca-rich mineralogy.

Note that Sprague et al. (2009) found that Mercury's reflectance spectra could not be fitted well using spectral libraries from end-member minerals and grain sizes that had previously worked well for the Moon and for some groups of meteorites. We concur that this demonstrates that the mineralogy of Mercury is distinct from e.g. the Moon and that alternative major and minor minerals are necessary to model the spectra and composition of Mercury. Interestingly, as this paper was prepared for submission, Sprague et al. (2009) found that including Mg or Ca rich garnets (perhaps indicative of deep rocks) improved their spectral fits. Garnet could be an alternative in our model to the feldspars as a source of aluminium, and if included would allow the Al/Na and Al/K ratios to vary more freely. Denevi et al. (2009) suggest that at least 15% of the surface of Mercury is covered by material derived from the lower crust or upper mantle, supporting an interpretation of garnet from deep rocks.

3. Mineralogical model of Mercury's average surface composition

Based on the available mineralogical information of Mercury's surface from spectroscopic observations, which we have outlined in the previous section, we designed a mineralogical model of Mercury's surface for our exosphere modelling. The exospheric observations of the few elements are used as an additional constraint to the mineralogical model. For modelling purposes we selected a group of end-member compositions that were then weighted to be consistent with the observational constraints (discussed below). Because of the large areas that are observed we do not necessarily expect a single rock-type to be present, and so geochemical self-consistency is not necessary (e.g. co-existence of silica-saturated and under-saturated minerals). As mentioned above our mineralogical model can be considered as a global model since the present knowledge of the surface mineralogy and its local variation is poorly understood. In any case, exospheric composition measurements, which are connected to the particle release processes, can be considered as sampling information from large surface areas. Thus, we consider our global mineralogical model adequate for the study of the contributions to the exosphere by sputtering, photo-stimulated desorption, and micro-meteorite impacts. The mineralogical model of the surface is largely based on the visible and IR observations mentioned above. In addition, we derive few constraints on the mineralogical composition from exospheric measurements for the three elements Na, K, and Ca.

Due to the lack of more data concerning a detailed mineralogy of Mercury's surface we base our mineralogical model mostly on three well established mineralogical groups: the feldspar group, the pyroxene group, and the olivine group. For defining our mineralogical model we use a mix of the end-members for each of the mineralogical groups. In addition, we added a few other minerals. By considering the constraints from the surface and exosphere observations we derive the mineralogical composition. Table 1 shows the derived mineralogical composition, together with the possible ranges for each mineral. Our mineralogical model is consistent with the preferred model of Goettel (1988). From this mineralogical model we get an average surface density of 3.11 g cm^{-3}. The mineralogical elements we consider, and their compositional constraints, are:

Feldspar group (about 27 mol%): feldspars are the most plausible source of alkali metals in the exosphere. We consider albite and K-feldspar to be the only end-members containing sodium and potassium, respectively. Feldspars may also contribute to the calcium signal (end-member anorthite) but we must consider that calcium is also found in pyroxenes. The feldspar group is assumed to be the only source of aluminium from the surface, thus, the Al abundance constrains the fraction of minerals of the feldspar group somewhat, such that the elemental Al abundance on the surface does not become unrealistically high compared to Mg and Si:

- Albite (about 17 mol%): only source of Na in exosphere, constrained by exospheric Na density observations.
- K-feldspar (0.39 mol%): only source of K in exosphere, constrained by exospheric K density observations, and the exospheric Na/K ratio.
- Anorthite (about 8.7 mol%): one of the sources of Ca in exosphere, constrained also by exospheric observations.

Pyroxene group (about 32 mol%): we consider the calcium, iron, and magnesium end-members of the pyroxene group, but iron and magnesium are also present in olvines.

- Wollastonite (about 2.9 mol%): one of the sources of Ca in exosphere, constrained by exospheric observations.
- Ferrosilite (about 0.4 mol%): constrained by IR spectroscopy giving low FeO fractions.
- Enstatite (about 29 mol%): source of Si, or SiO and Mg.

Table 1
Derived mineralogical composition of Mercury's surface used in our calculations of the exosphere. The last column gives the possible range of mineral abundances in the mineralogical model.

Mineral	Chemical composition	Mineral abundance (mol%)	Range (mol%)
Iron/nickel metal	Fe, Ni	0.07	0.04–0.15
Troilite	FeS	0.15	0–0.5
Daubreelite	$FeCr_2S_4$	0.15	0–0.3
Oldhamite	CaS	0.15	0–0.3
Sphalerite (end-member)	ZnS	0.58	0–1
Feldspar group			
Albite	$NaAlSi_3O_8$	17.44	13–21
K-feldspar	$KAlSi_3O_8$	0.39	0.2–0.7
Anorthite	$CaAl_2Si_2O_8$	8.72	6.7–11
Ilmenite	$FeTiO_3$	0.07	0.02–0.15
Apatite	$Ca_5(PO_4)_3OH$	1.45	0–2
Pyroxene group			
Wollastonite	$CaSiO_3$	2.91	2.4–3.5
Ferrosilite	$Fe_2Si_2O_6$	0.36	0.1–0.5
Enstatite	$Mg_2Si_2O_6$	29.06	24–34
Olivine group			
Fayalite	Fe_2SiO_4	2.18	1.7–2.7
Fosterite	Mg_2SiO_4	36.33	31–41

Olivine group (about 39 mol%): iron and magnesium may also be present in olvines so we must also consider fayalite and forsterite, consistent with spectroscopy suggesting Mg-rich and Fe-poor:

- Fayalite (2.18 mol%): major contributor of FeO in our model, but FeO abundance is severely constrained by IR spectroscopy.
- Fosterite (36.33 mol%): major contributor to olivine (Sprague et al., 1994, 2007).

Metallic iron and nickel (0.07 mol%): nano-phase iron formed during the regolith maturation process due to micrometeorite impacts and solar wind sputtering of the surface. Abundance is constrained by IR spectroscopy.

Sulphides (1.03 mol%): the abundance of sulphides on the surface of Mercury is not constrained by available observations. In 1992 Harmon and Slade (1992) discovered radar bright spots near the poles of Mercury. The high radar reflectivity was initially attributed to water ice because of the possibility of permanently shaded areas at the poles. However, the presence of elemental sulphur has been suggested as the volatile material in the cold areas near the poles (Sprague et al., 1995). Based on measurements on mineral analogues for Mercury's surface about 6 wt% sulphides might be expected in the basaltic crust (Burbine et al., 2002):

- Troilite (0.15 mol%): sulphides (Burbine et al., 2002).
- Daubreelite (0.15 mol%): sulphur bearing mineral, only contributor of chromium.
- Oldhamite (0.15 mol%): sulphides (Burbine et al., 2002).
- Sphalerite (0.58 mol%) end-member.

The claim by Kerber et al. (2009) of higher than previously thought volatile contents in Mercury (at least in the past) based on the observation of pyroclastic deposits gives more plausibility to the presence of sulphur in some form on the surface.

Ilmenite (0.07 mol%): ilmenite is included as the only titanium-bearing mineral. IR spectroscopy on Mercury suggests a very low abundance, however, ilmenite is observed in lunar samples and so is included here by analogy despite the recent report by Sprague et al. (2009) that their preferred compositions did not include ilmenite but rather rutile as an opaque titanium containing phase.

Apatite (1.45 mol%): apatite serves as a possible source of halogens and hydroxyl species. It may be the source of OH in the exosphere of non-volatile origin. Recently, hydroxyapatite has been identified in lunar samples (McCubbin et al., in press). OH of volatile origin would be from the photo-dissociation of H_2O in the exosphere, with the water (from meteorites, comets, or permanently shaded regions) being thermally desorbed. An alternative to apatites as a source of hydroxyl would have been amphiboles as suggested (and observed for some regions) by Sprague et al. (2009).

3.1. Compositional modelling of Mercury's surface

From the mineralogical model we obtain an elemental composition of Mercury's surface. To derive the elemental surface composition we compare the widely used classical additive composition modelling method (e.g. Sprague et al., 2009) with a more accurate, but in planetology novel multiplicative method (with and without fixed Ca fraction). These three compositions are shown in Table 2.

The compositional nature of the vectors of percentages implies that two main principles should be verified by any analysis: scale invariance and subcompositonal coherence (Aitchison, 1986). Whereas the "multiplicative" (i.e., *Log-ratio*) approach satisfies both principles, the "additive" (i.e., *Euclidean*) methodology does not. There is a special publication of the Geological Society where both theoretical and practical advantages of multiplicative approach are explained in detail.

To be sure that the composition modelling results of the previously used and simpler additive method differs not much from the results obtained by the more realistic multiplicative method, we compare both approaches. Kolb et al. (2006) applied the same method for compositional data analysis on chemical compositions of Martian surface materials to unravel scenarios of past and present weathering and to evaluate the role of meteoritic accumulation. Moreover, several studies where some of them focus in its theoretical properties (e.g., Martín-Fernández and Thió-Henestrosa, 2006) and others in its practical applications (e.g., Thomas and Aitchison, 2006) have recently been published by the Geological Society and indicate that the multiplicative (i.e., *Log-ratio*) composition modelling methodology yields in some

Table 2
Elemental abundance of Mercury's surface adapted from the literature compared to the composition modelled with the additive and multiplicative methods (in atom percent at the surface).

Comp. number	Model composition	O	Na	Mg	Al	Si	P	S	K	Ca	Ti	Cr	Fe	Ni	Zn	OH
	Preferred model (Goettel, 1988)	56.9	0.24	25.0	1.09	13.3				2.48	0.052		0.97			
	Refractory-rich model (Goettel, 1988)	55.8	0.0	23.6	3.52	9.78				7.33	0.162		0.0			
	Volatile-rich model[a] (Goettel, 1988)	56.7	0.64	21.5	0.69	13.4				1.45	0.031		5.61			
	Chondrite model (Morgan & Anders, 1980)	57.5	0.037	22.9	1.35	14.2			0.032	2.55	0.073		1.37			
	Equilibrium condensation (Wood et al., 1981)	56.4	0.0	26.0	1.93	11.7				3.96	0.104		0.019			
	Equilibrium condensation, use of feeding zones (Wood et al., 1981)	56.8	0.0	26.0	1.43	12.7				3.00	0.077		0.014			
	Dynamically mixed (Wood et al., 1981)	56.2	0.0	29.3	0.908	11.9				1.77	0.0		0.0			
	Collisionally differentiated (Wood et al., 1981)	55.7	0.0	32.2	0.0	11.4				0.737	0.0		0.0			
	Vaporisation model (Fegley & Cameron, 1987)	55.9	0.0	23.4	3.8	9.67				7.05	0.158		0.0			
1	Additive model	58.61	1.34	16.2	2.71	17.4	0.208	0.519	0.030	1.670	0.015	0.042	0.872	0.004	0.291	0.069
2	Multiplicative model without Ca fixed	58.80	1.34	16.1	2.64	17.4	0.208	0.529	0.030	1.269	0.015	0.042	1.279	0.004	0.291	0.069
	Multiplicative model with Ca=1.67%	59.42	1.32	15.8	2.62	17.3	0.268	0.591	0.030	1.670	0.014	0.041	0.611	0.004	0.285	0.069

[a] The H_2O fraction was specified as "a lot" by Goettel (1988), but was not considered here because available observations show no indication of "a lot" of water.

cases more accurate results compared to the additive (i.e., *Euclidean*) method.

These three compositions are shown in Table 2 together with results from earlier models of the mantle composition (Morgan and Anders, 1980; Wood et al., 1981; Fegley and Cameron, 1987; Goettel, 1988), which assumed a formation or evolution process of Mercury that resulted in a given mineralogical composition of mantle and core. The difference of our approach to these earlier models is that we took all available observational data (visible and IR spectroscopy and exospheric composition) to derive (constrain) a global mineralogical composition of the surface, actually the composition of the upper present surface layer that has undergone space weathering. For the major elements, the composition does not vary much between the formation models and our model derived from observations. Except, the Na abundance we derive is higher than in the mantle models, and our Mg abundance is lower, possibly indicating that our model composition resembles the crust. For minor elements these variations are much larger, and knowledge of their abundance would allow distinguishing between the models. Thus, it will be important to measure the low abundance elements on the surface to constrain the mineralogical composition.

3.1.1. Classical additive method

Having chosen end-members for our mineralogical model we directly have the chemical composition of the minerals, which is given in Table 1. Depending on the abundance of each mineral we thus derive an average elemental composition of the surface. By quantitatively modelling the release process of each element in the exosphere (discussed below) we can relate the exospheric density (the exospheric surface density or the column density) to the elemental concentration at the surface.

The various observational inputs and the modelling are combined in one large calculation, which is schematically shown in Fig. 1. We start out with a set of minerals and their abundances. From this we calculate the elemental abundance of the surface and the sputter yields for all elements for the chosen mineral abundances. The sputter yields and the elemental abundances are inputs to the calculation of the exospheric densities. Other release processes, such as MIV and PSD, are also considered (the latter only when applicable). We tried to duplicate the external conditions during the observations in our calculations to the extent they are known or can be estimated, and the resulting exospheric densities are then compared to the observations. The elemental abundances at the surface have to be adjusted if the resulting exospheric densities do not match with observations. Such an adjustment is done by changing the mineral abundances. This is an iterative process until all available constraints are satisfied. As an additional constraint we have the Na/K ratio and the surface density. Although there are a limited number of observational constraints, the solution for the mineralogical composition is quite robust.

For reproducing the ground-based exosphere observations of the Na, K (e.g., Killen et al., 2007), and Ca (Bida et al., 2000) exosphere we estimate the surface contents of these elements to be 1.341, 0.03, and 1.67 at%, respectively. The Na/K elemental ratio we obtain in our model for the surface material is about 45, which gives a Na/K ratio in the exosphere of 23 (comparing the column densities). This corresponds to the lower range of Na/K ratios obtained from exosphere observations (Potter et al., 2002; Killen et al., 2007). Based on their model of the surface mineralogy Cremonese et al. (2005) derived a Na/K ratio of 49 and a Na fraction on the surface of 3.7 wt%. However, a Na/K ratio of 45 or 49 at the surface is higher than for many other objects in the solar system where values between 10 and 20 are found (see review by Killen et al., 2007). Potter et al. (2002) speculated that the Na/K on Mercury's surface might be the same as for other solar system objects, but differences in the release process of Na and K into the exosphere accounts for the high ratio in the exosphere. In our model the K-feldspar is the only source for K in the exosphere. However, if we were to increase the abundance of K-feldspar in the model by a factor of 2 to get a Na/K of about 20 on the surface, the increased calculated exospheric density of K would exceed the observed values. Also the resulting Na/K ratio in the exosphere would be below the observed range. Decreasing the albite content by a factor of 2 would be in conflict with several optical observations. Mura et al. (2009) showed in a recent study that the Na release into the exosphere can be enhanced by the combined effect of sputtering and PSD.

3.1.2. Multiplicative method

The closed nature of compositional data, i.e., the constraint that component concentrations sum to 100% in an analysis, bears important implications for its statistical analysis. Above, our analysis is based on simple correlation methods and Euclidean space geometry. This commonly used method does generally not fully exploit the potential of the available data. The correlation coefficients between fixed pairs of elements and the Euclidean distance between two samples are both substantially influenced by the normalisation to a constant sum. For investigating the
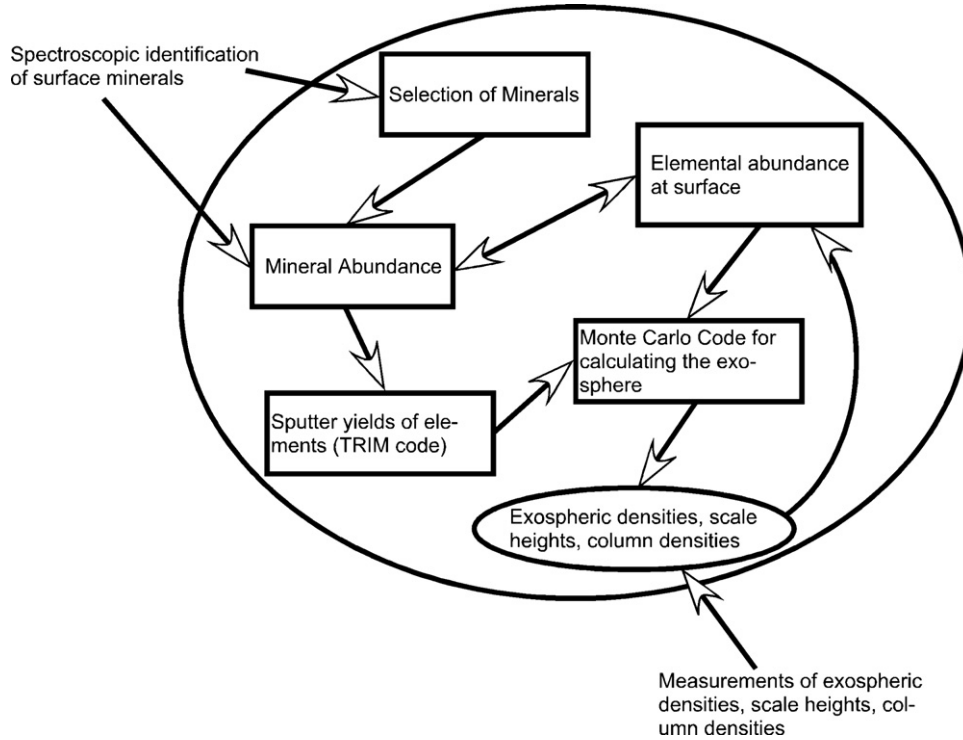
Fig. 1

possible variation of elemental composition due to the classical additive statistical technique we apply also a multiplicative method, which was developed by Aitchison (1986) and which is used in various problems related to composition modelling (e.g., Martín-Fernández and Thió-Henestrosa, 2006; Thomas and Aitchison, 2006).

In the traditional Euclidean space one is dealing with absolute compositional values of individual entries. To account for the relative nature of compositional data, ratios among entries are considered rather than absolute values. This principle is known as *scale invariance* (Aitchison, 1986). For example, as pointed out before, the log-ratio methodology for compositional data analysis introduced in Aitchison (1986) has successfully been employed for the interpretation of chemical data returned from the Martian surface (Kolb et al., 2006). A composition can be defined as a collection of D non-negative measurements, which sum to unity (or 100%) per weight, volume, or abundance. Such constraints are obeyed by the Simplex space geometry, which represents a D-dimensional analogue of a triangle, in contrast to the D-dimensional orthogonal Euclidean space geometry. If only a subset of the chemical constituents that are present in a sample is represented in a closed form, i.e., normalised to a constant sum (e.g. 100%), such a collection of measurements is referred to as a *subcomposition*. In general, measured chemical compositions should be considered as subcompositions in the sense of Aitchison (1986).

The closed nature of compositional data causes the dependence of individual compositional entries on each other. To model an exchange of chemical compositions Aitchison and Barceló-Vidal (2002) proposed the so-called *perturbation* mechanism, symbolized by the ⊕ sign. Eq. (1) shows its application. By means of perturbation vector $\mathbf{p}$ the chemical composition $\mathbf{C}$ yields the chemical composition $\mathbf{C}^*$,

$$\mathbf{C}^* = \mathbf{p} \oplus \mathbf{C} = Cl([p_1 c_1, p_2 c_2, \ldots, p_D c_D])$$

$$= \left[\frac{p_1 c_1}{\sum_{i=1}^{D} p_i c_i}, \frac{p_2 c_2}{\sum_{i=1}^{D} p_i c_i}, \ldots, \frac{p_D c_D}{\sum_{i=1}^{D} p_i c_i} \right], \tag{1}$$

whereby $Cl(\cdot)$ denotes the closure or normalisation operation. The components of the perturbation vector are a measure of change for the same parts of compositions linked by this vector. Using log-ratio methodology this change is modelled in a multiplicative way, rather than in the additive way applied by the traditional statistical techniques. Eq. (2) shows the compositional difference vector $\mathbf{p}$ between the compositions $\mathbf{C}^*$ and $\mathbf{C}$:

$$\mathbf{p} = \mathbf{C}^* \oplus \mathbf{C}^{-1} = Cl\left(\left[\frac{c_1^*}{c_1}, \frac{c_2^*}{c_2}, \ldots, \frac{c_D^*}{c_D}\right]\right), \quad \mathbf{C}^{-1} = Cl\left(\left[\frac{1}{c_1}, \frac{1}{c_2}, \ldots, \frac{1}{c_D}\right]\right), \tag{2}$$

whereby $\mathbf{C}^{-1}$ is the inverse of composition $\mathbf{C}$. The inverse of one composition can be generally considered in the Simplex, without regard to their definition as chemical composition or compositional vector. The inverse $\mathbf{C}^{-1}$ vector is the link between $\mathbf{C}$ and the *uniform* composition. The uniform composition or *neutral* perturbation vector in the D-dimensional space Simplex is the composition $\mathbf{e} = Cl(1, 1, \ldots, 1) = (1/D, 1/D, \ldots, 1/D)$. This uniform composition $\mathbf{e}$ corresponds to the barycentre of the Simplex and plays the same role as the origin or null vector in the Euclidean space.

Combination of the concept of perturbation mechanism and inverse of composition allows to model "step-by-step" the change between two compositions $\mathbf{C}^*$ and $\mathbf{C}$. For example, one could consider that one composition $\mathbf{C}$ moves to another composition $\mathbf{C}^*$ applying the "2 steps" perturbation mechanism with the perturbation vector:

$$\mathbf{p} = \left[\sqrt{\frac{c_1^*}{c_1}}, \sqrt{\frac{c_2^*}{c_2}}, \ldots, \sqrt{\frac{c_D^*}{c_D}}\right]. \tag{3}$$

That is, $\mathbf{C}^* = \mathbf{p} \oplus (\mathbf{p} \oplus \mathbf{C}) = \mathbf{p}^2 \oplus \mathbf{C}$. Note that the element $\mathbf{p} \oplus \mathbf{C}$ is the *geometric* centre between both compositions $\mathbf{C}^*$ and $\mathbf{C}$. Eq. (4) shows that the geometric centre corresponds to the closure of the geometric mean of both compositional vectors:

$$\mathbf{p} \oplus \mathbf{C} = Cl\left(\left[\sqrt{\frac{c_1^*}{c_1}} c_1, \sqrt{\frac{c_2^*}{c_2}} c_2, \ldots, \sqrt{\frac{c_D^*}{c_D}} c_D\right]\right)$$

$$= Cl([\sqrt{c_1^* c_1}, \sqrt{c_2^* c_2}, \ldots, \sqrt{c_D^* c_D}]). \tag{4}$$

Eq. (5) shows that this procedure can be easily generalised to produce any intermediate composition **C** between **C*** and **C**:

$$\mathbf{C}^{**} = Cl([(c_1)^{\alpha}(c_1^*)^{1-\alpha},(c_2)^{\alpha}(c_2^*)^{1-\alpha},\ldots,(c_D)^{\alpha}(c_D^*)^{1-\alpha}]), \quad \text{for } 0 \le a \le 1. \tag{5}$$

This expression is a particular case of the power transformation (Aitchison, 1986) combined with the perturbation mechanism. It is well known in composition modelling that another important principle of compositional data analysis is *subcompositional coherence*. The subcompositional coherence principle is crucial for illustrating how traditional statistical techniques could produce misleading results. In Appendix A we show a simple example where the traditional additive procedure and the perturbation mechanism for producing intermediate composition are compared in terms of this principle.

The calculation of intermediates between two compositions by using the perturbation mechanism can be easily generalised to the case of the intermediates between *n* compositions $\mathbf{C}_1$, $\mathbf{C}_2, \ldots, \mathbf{C}_n$. In the present study we made intermediate compositions by using the perturbation mechanism procedure for the chemical data given in Table 1. Chemical subcompositions of Mercury's minerals of the abundance 15 elements (O, Na, Mg, Al, Si, P, S, K, Ca, Ti, Cr, Fe, Ni, Zn, OH) were produced. The values of the parameter α in Eq. (5) are deduced from the mineral abundances kept in Table 1. Note that when one produces intermediate compositions of those elements, which are not simultaneously present in some compositions, they appear as zero in this composition. To avoid the zero-effect in the perturbation mechanism procedure, the intermediate subcomposition is calculated and then the rest of the elements are imputed.

For example, when one calculates the intermediate composition in the Pyroxene group one deals with the minerals Ca Si O$_3$; Fe$_2$ Si$_2$ O$_6$; and Mg$_2$ Si$_2$ O$_6$. Then the compositions are formed by the elements (Si, O, Ca, Fe, Mg). For this mineral group, the intermediate composition is produced applying the perturbation mechanism to the subcomposition (Si, O) and then, imputing the rest of elements to obtain the full composition. This imputation was made applying the imputation method introduced in Martín-Fernández et al. (2003). This method of imputation guarantees that the ratios between the elements are preserved. Following this strategy the alternative estimates for the surface composition is obtained and compared with the simple additive correlation method shown in Table 2. One can see that the main difference between the composition modelled with the additive and the multiplicative methods is the amount of Fe. In the multiplicative method the ratio of Na/K is kept constant to a value of about 44 in all the cases. Because Ca is most likely sputtered from the surface (Bida et al., 2000) and an amount of 1.67 at% reproduces the observed exosphere column density very well (Wurz and Lammer, 2003) one can also fix this value. By doing so, the multiplicative method gives only slightly lower Fe contents compared to the additive method. But if Ca is taken not as a constant one can see that the Ca composition would be lower and the Fe part much higher. In such a case the composition would not be in agreement with the models of Goettel (1988).

3.1.3. Additive versus multiplicative composition modelling approach

In spite of that the absolute differences between the results produced by the additive method and the multiplicative are small, there are relative differences between some trace elements that are large (e.g., S when one fixes the Ca element). These effects can be explained because the most abundant minerals shown in Table 1 are Albite, Enstatite, and Fosterite, which are mainly composed by the main chemical elements O, Mg, and Si (see Table 2). In addition, the different effect of both methods is distributed between the 15 elements in the composition not causing large absolute differences in the trace elements. One should note that the subcomposition formed by the trace elements in some minerals like troilite, oldhamite, sphalerite (see Table 1) is close to the barycenter of the simplex ($\mathbf{e} = [1/D, \ldots, 1/D]$). As stated by Martín-Fernández and Bren (2001), when the data are near to the barycenter both Euclidean and Log-ratio tools produce approximate results. From our results and analysis of the two composition modelling approaches we can conclude that in Mercury's case the simpler additive method yields also accurate results, which can also be applied for future surface–exosphere interaction studies.

4. Sputtering of Mercury's surface minerals

We consider particle sputtering as one of the most interesting surface release processes because it releases all elements from the planet's surface minerals into the exosphere by reproducing more or less the local surface composition on an atomic level. When a surface is freshly exposed to ion bombardment, preferential sputtering of the different elements of a compound will lead to an enrichment of those elements with low sputtering yields in the top-most atomic layers of the surface. However, when a steady-state sputtering situation is reached, the composition of the flux of sputtered atoms will reflect the average bulk composition (Betz and Wehner, 1983). Therefore, exospheric densities resulting from particle sputtering, when operative in a steady-state situation, will give us quantitative compositional information about all elements of the bulk surface, including the refractory elements. Such a steady-state situation is reached after a solar wind exposure of the surface of between 2 and 20 days corresponding to solar wind proton fluxes of 10^{12}–10^{13} m^{-2} s^{-1}, respectively, which is a very short period compared to the average residence times of regolith grains on Mercury's surface, which has been estimated to be 1.5×10^5 years (Killen et al., 2007).

The details of the calculation of the particle release by sputtering are given in the earlier publications (Wurz and Lammer, 2003; Wurz et al., 2007). The flux Φ_i of particles sputtered from the planetary surface can be calculated as

$$\Phi_i = \Phi_{\text{ion}} Y_i^{\text{tot}} = \Phi_{\text{ion}} Y_i^{\text{rel}} C_i, \tag{6}$$

where Φ_{ion} is the ion flux onto the surface and Y_i^{tot} the total and Y_i^{rel} the relative sputter yield of species *i* from the surface, i.e., the elemental mixture of the atomic abundance C_i of species *i* on Mercury's surface (see Table 2). We calculated the total sputter yield, Y_i^{tot}, for all species *i* for the two reference surface compositions (composition models 1 and 2 in Table 2) by using the TRIM.SP software (Biersack and Eckstein, 1984; Ziegler et al., 1984; Ziegler, 2004). Depending on the abundance of a species in Mercury's surface composition between 75,000 and 1,700,000 projectile ions were simulated with TRIM.SP to ensure good statistics. As projectile ions we used a mixture of protons and alpha particles, 95% and 5%, respectively, which represents normal solar wind conditions. The sputter yields are low, less than 0.1 surface atoms are sputtered from a grain/rock per impacting solar wind ion. The reason for the low sputter yields is that the solar wind is mostly composed of protons, which have a low sputter yield because of their small mass. The 5% alpha particles typically contribute 30% to the total sputter yield. Heavy solar wind ions have only total abundance of about 0.1% in the solar wind (e.g., Wurz, 2005, and references therein). We find that oxygen and iron ions of the solar wind contribute not more than about 1% to the sputter yield, other heavy ions even less.

Therefore, we do not consider the contribution of heavy ions to the sputtered flux. However, during coronal mass ejections the abundance of heavier ions may be enhanced considerably (Wurz et al., 2003) and their contribution to the sputter yield may become significant.

It has been argued that the internal energy associated with the high charge states of the heavy ions in the solar wind significantly increases their sputter yield (Shemansky, 2003). In Appendix B we review the pertaining laboratory data and come to the conclusion that there is no increased sputter yield for heavy solar wind ions with their typical charge states for typical planetary surfaces.

We calculated the sputter yields for a sputter ion velocity range from 300 to 800 km s^{-1} to cover the typical variation of solar wind conditions in our model. However, the sputter yields do not vary much over this range similar to the lunar surface (Wurz et al., 2007) and we therefore present only data for solar wind speeds of 440 km s^{-1}. The velocity dependence is such that the maximum of the sputter yield typically results from solar wind speeds in the range between 300 and 500 km s^{-1}. These calculated sputter yields are for solid grains. The porosity of the regolith surface, which effectively reduces the sputter yield (Cassidy and Johnson, 2005), is included later in the calculation. In our calculations we use a regolith porosity of 30%, which reduces the total sputter yield for solar wind to about 0.07 sputtered atoms per incident solar wind ion. With this sputter yield and the integrated ion flux onto Mercury's surface of 1.1×10^{25}–3×10^{26} s^{-1} we get a global sputter rate of $(0.36$–$9.8) \times 10^{-11}$ m a^{-1}, which is comparable to the lunar value of 4×10^{-11} m a^{-1}.

The total sputter flux Φ_i of species i is

$$\Phi_i = N_i(0)\langle v_i \rangle, \tag{7}$$

where $N_i(h)$ exospheric density profile with altitude h, and $N_i(0)$ the exospheric particle density at the surface, and $\rangle v_i \langle$ is the average velocity of sputtered particles. Combining Eqs. (6) and (7) we calculate the exospheric density at the surface for species i as

$$N_i(0) = \Phi_{\mathrm{ion}} Y_i^{\mathrm{tot}} \frac{1}{\langle v_i \rangle}. \tag{8}$$

We use $N_i(0)$ in the Monte-Carlo calculation as a starting point for the calculation of the density profile from the sputtering process for the modelled surface composition. We can easily integrate the exospheric density profile to obtain the column density (or the tangential column density), which is the typical measurement obtained from telescopic observations of the exosphere. In conclusion, if we know the flux of ions impinging on the planetary surface, Φ_{ion}, then with the sputter yields Y_i^{tot} we can calculate the sputtered flux, the surface density, the density profile, and the column density *ab initio* and compare these numbers with the observations.

The average release velocity is derived from the sputter distribution (see Wurz et al., 2007). If we take oxygen as an example, with a surface binding energy of $E_b = 2.0$ eV, we obtain an average release velocity of $\langle v_i \rangle = 11.57$ km s^{-1}, which exceeds Mercury's escape speed of 4.250 km s^{-1} considerably. Note that the most probable velocity is $v_{\mathrm{mp}} = \sqrt{E_b/m_2}$ (with m_2 the mass of the sputtered atom), which is lower than the average release speed by a factor of about 3.3. However, the most probable velocity is $v_{\mathrm{mp}} = 3.47$ km s^{-1}, which means that only a fraction of the sputtered oxygen escapes from the gravitational field of Mercury. The heavier the element the more unlikely it will escape from Mercury's exosphere, especially when considering the mass dependence in the average release velocity (Wurz et al., 2007), which is illustrated in Fig. 2 where the energy corresponding to the escape speed is indicated in the energy distribution of sputtered atoms.
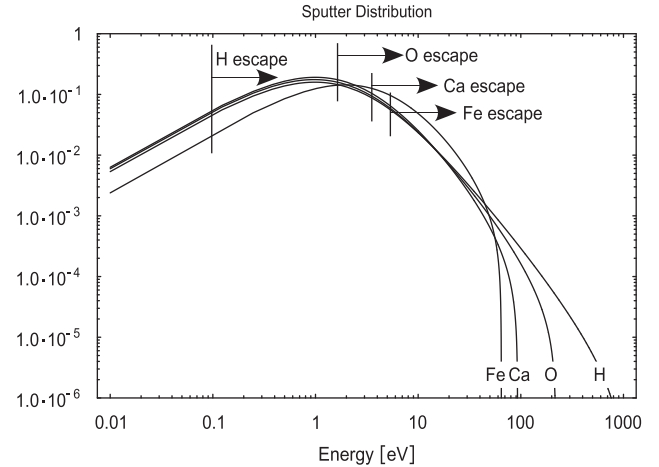

Fig. 2

5. Calculated exospheric densities

We calculate millions of particle trajectories for each species and each release process (sputtering, photon stimulated desorption, and micro-meteorite impact vaporisation) using a Monte-Carlo simulation code, which has been described earlier (Wurz and Lammer, 2003; Wurz et al., 2007). The mathematical description for the release processes is given in Appendix C. Each particle trajectory starts with an initial energy and angle selected at random from the prescribed distribution for the particular ejection mechanism. The particle trajectory is then calculated for discrete altitude steps. The particle either falls back to the surface, or gets ionised somewhere on its trajectory and is thus lost from the neutral exosphere, or leaves the calculation domain, which is given by the Hill radius in our model. When a particle falls back onto the surface we assume perfect sticking. Since we are concerned with mostly refractory elements and chemically active elements (e.g., oxygen) in this study assuming perfect sticking is reasonable. Na is the only known exception where a temperature dependent sticking coefficient less than unity has been observed (Yakshinskiy et al., 2000). The lower sticking coefficient for Na means that from the Na falling back to the surface there is a fraction returning to the exosphere as thermalised gas. Thus, we underestimate the Na exospheric density near the surface (within the first 100 km) for sputtering and MIV, but the column densities are hardly affected. From the calculated trajectories we derive the exospheric density profiles and column densities for the applicable release processes. Escape from Mercury's gravitational field and loss due to photo-ionisation were an integral part of the trajectory calculation. We did not perform a new calculation of the density profiles of volatile species in Mercury's exosphere (H, H_2, He, Ne, N_2, CO, O_2, Ar, and CO_2), since we consider the earlier density profiles from Wurz and Lammer (2003) still valid.

For sputtering, we studied various solar wind situations with different solar wind speeds and flux to compare to the different conditions for which exospheric observations were reported. Results are presented here only for the case of $v_{\mathrm{SW}} = 440$ km s^{-1} and the solar wind flux is $f_p = 4.1 \times 10^{12}$ m^{-2} s^{-1}, which is in the middle of the range of predicted ion fluxes of 10^{12}–1×10^{13} m^{-2} s^{-1} onto Mercury's surface (Killen et al., 2007). In general, sputter yields on Mercury are very similar to the Moon, which were reported in detail in Wurz et al. (2007). The velocity dependence of the sputter yield is weak, and the maximum of the sputter yield is approximately for particles impinging at the surface with 1 keV/nuc, i.e., typical solar wind speeds. The sputtered fluxes for each species, and thus the associated exospheric densities, scale linearly with the ion flux onto the surface. The density profiles

for sputtering resulting from these calculations for the composition models #1 and #2 are shown in Fig. 3, top panels. Overall, the calculated exospheric densities for solar wind sputtering are low, and the sum of all calculated elements gives an exospheric surface density of about 4×10^7 m^{-3}, which is much lower than the total density of Mercury's exosphere at the surface of 10^{12} m^{-3} (upper limit, corresponds to 10^{-10} mbar thermal gas). Most of the exospheric species are volatiles released thermally or via PSD

from Mercury's surface and thus have a low scale height in the atmosphere (Wurz and Lammer, 2003), e.g. $h_H = 910$ km, $h_{He} = 210$ km, $h_{OH} = 73$ km, and $h_{N_2} = 50$ km, for thermal release at the sub-solar point ($T = 480$ K), and for PSD release $h_{Na} = 190$ km and $h_K = 60$ km, again at the sub-solar point. Sputtered atoms have more energy than thermally released species and thus a significantly larger scale height and will be accessible to investigation by orbiting spacecraft. Typical scale heights are
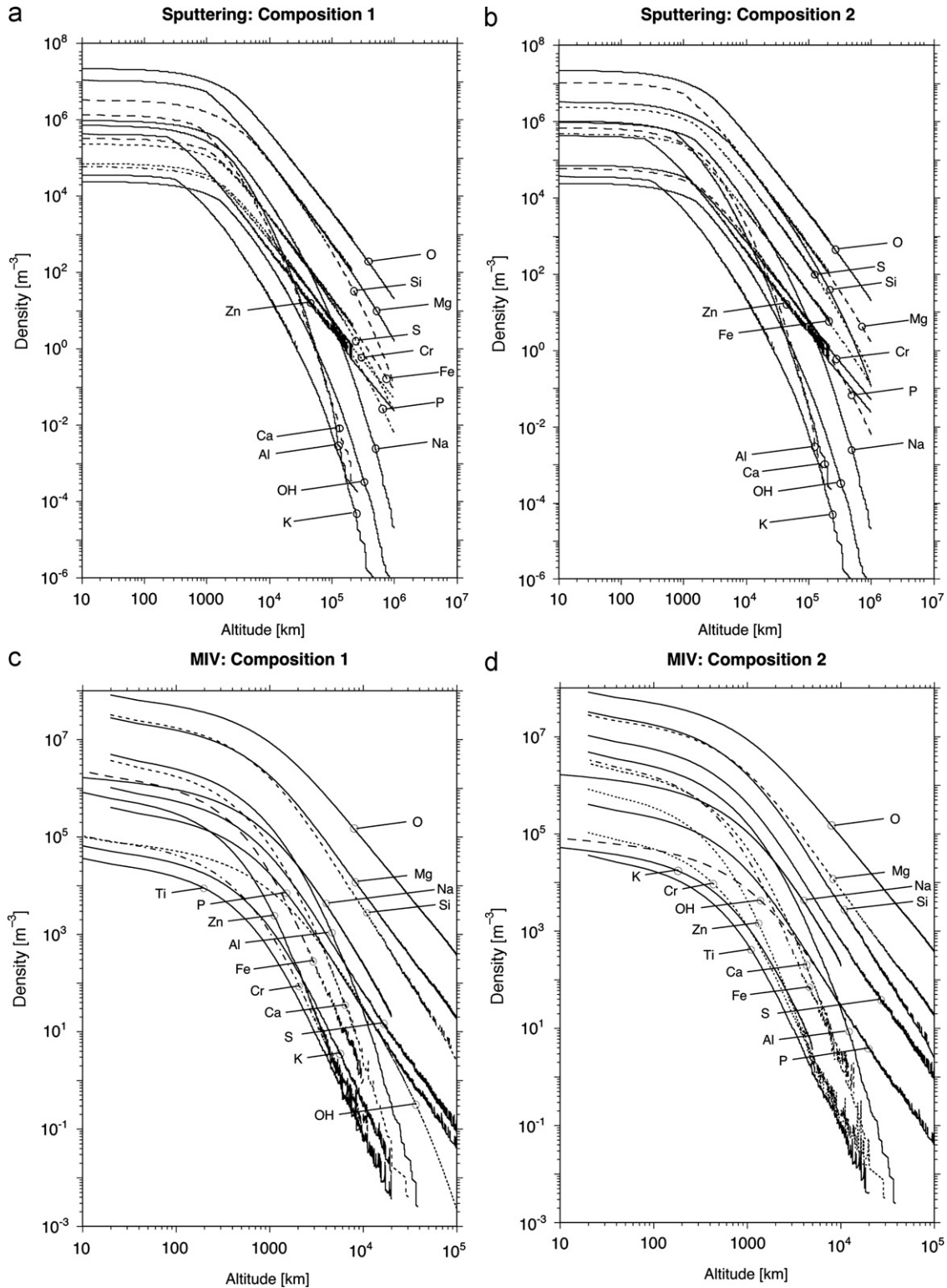

Fig. 3

$h_O = 1600$ km, $h_{Mg} = 1300$ km, and $h_{Ca} = 890$ km. Sputtered atoms start to dominate the exosphere at altitudes around 1000 km, with the exception of thermally released H_2 and He, which are sufficiently light and abundant to be observed at higher altitudes. Note that H_2 has not been detected in Mercury's exosphere so far, but is expected to be present in significant quantities (Killen and Ip, 1999).

Table 3 gives the expected exospheric densities at the surface and the column densities for typical particle release conditions. For sputtering, the density values and the associated density profiles we present here are much lower than what we published earlier (Wurz and Lammer, 2003), since the earlier values were calculated using upper limits for the exospheric densities at the surface reported by Killen and Ip (1999), in contrast to the present values that are derived in a self-consistent manner from the surface mineralogy. Ca is considered to be contributed to the exosphere by sputtering (Bida et al., 2000; Killen et al., 2007). Our

Ca values agree reasonably well with the literature results (Bida et al., 2000; Killen et al., 2005) since these were used as constraints in our derivation of the surface mineralogy. Upper limits for Ca reported earlier (Sprague et al., 1993; Killen and Ip, 1999) are much higher than the present measurements and our model results. McClintock et al. (2009) reported the discovery of Mg in Mercury's exosphere with the UV spectrometer during the second MESSENGER flyby. So far only radiances are given, but no conversions to densities or column densities are available. Thus, we have to await their analysis before we can compare it to the results of our calculation.

Reported exospheric Na densities (e.g. Potter and Morgan, 1997; Schleicher et al., 2004) and most recently by MESSENGER (McClintock 2008a, 2009) are typically two orders of magnitude larger than what we get using sputtering or MIV. Also the observed exospheric K densities (Potter et al., 2002) are higher by two orders of magnitude than the K densities we derive from

Table 3
Results from the calculated exospheric densities are given for the sputter process (SP), and the photon-stimulated desorption process (PSD).

Element	Release process	Composition #1		Composition #2		Literature values	
		Surface density (m^{-3})	Column density (m^{-2})	Surface density (m^{-3})	Column density (m^{-2})	Surface density (m^{-3})	Column density (m^{-2})
O	SP	2.20×10^7	4.38×10^{13}	2.20×10^7	4.39×10^{13}	$4.4 \times 10^{10a,i}$	3×10^{15a}
O	MIV	8.21×10^7	3.43×10^{13}	8.23×10^7	3.44×10^{13}	–	–
OH	SP	2.42×10^4	3.54×10^{10}	2.42×10^4	3.54×10^{10}	1.4×10^{9g}	$1 \times 10^{14a, g}$
OH	MIV	9.96×10^4	2.28×10^{10}	9.96×10^4	2.98×10^{10}	–	–
Na	SP	9.66×10^5	1.39×10^{12}	9.66×10^5	1.39×10^{12}	–	–
Na	MIV	2.25×10^6	5.12×10^{11}	2.25×10^6	5.12×10^{11}	–	$(2.5–8.5) \cdot 10^{14h}$
Na	PSD	1.97×10^9	3.70×10^{14}	1.97×10^9	3.70×10^{14}	5.0×10^{8e} $(1.7–3.8) \cdot 10^{10g}$	3.4×10^{14f} 2×10^{15g} $(3–10) \times 10^{14j}$
Mg	SP	1.09×10^7	1.52×10^{13}	1.08×10^7	1.51×10^{13}	$7.5 \times 10^{9a, g}$	$3.9 \times 10^{14a, g}$
Mg	MIV	2.79×10^7	8.44×10^{12}	2.77×10^7	8.37×10^{12}	–	–
Al	SP	7.23×10^5	8.36×10^{11}	7.04×10^5	8.15×10^{11}	$6.54 \times 10^{8a, g}$	$3.0 \times 10^{13a, g}$
Al	MIV	4.93×10^6	1.06×10^{12}	4.81×10^6	1.04×10^{12}	–	–
Si	SP	3.30×10^6	6.66×10^{12}	3.30×10^6	6.66×10^{12}	2.7×10^{9a}	1.2×10^{14a}
Si	MIV	3.23×10^7	8.53×10^{12}	3.23×10^7	8.53×10^{12}	–	–
P	SP	5.94×10^4	1.05×10^{11}	5.94×10^4	1.05×10^{11}	–	–
P	MIV	4.05×10^5	9.95×10^{10}	4.05×10^5	9.95×10^{10}	–	–
S	SP	2.32×10^5	3.80×10^{11}	2.36×10^5	3.88×10^{11}	$5 \times 10^{9a, g}$	$2.0 \times 10^{14a, g}$
S	MIV	1.03×10^6	2.45×10^{11}	1.05×10^6	2.50×10^{11}	–	–
K	SP	3.68×10^4	2.26×10^{10}	3.68×10^4	2.26×10^{10}	–	–
K	MIV	6.57×10^4	1.04×10^{10}	6.57×10^4	1.04×10^{10}	–	–
K	PSD	3.03×10^8	1.60×10^{13}	3.03×10^8	1.60×10^{13}	3.3×10^{8g} 5.0×10^{8g}	2.0×10^{13g}
Ca	SP	1.36×10^6	1.22×10^{12}	1.04×10^6	9.29×10^{11}	$3.87 \times 10^{8a, g}$ $< 2.39 \times 10^{8b}$	$< 1.2 \times 10^{13a, g}$ $< 7.4 \cdot 10^{12b}$ 1.1×10^{12c} $(0.5–1.8) \times 10^{12d}$
Ca	MIV	3.70×10^6	6.48×10^{11}	2.81×10^6	4.93×10^{11}	–	–
Ti	SP	2.03×10^4	3.25×10^{10}	2.03×10^4	3.25×10^{10}	–	–
Ti	MIV	3.63×10^4	6.11×10^9	3.63×10^4	6.11×10^9	–	–
Cr	SP	7.19×10^4	1.08×10^{11}	7.19×10^4	1.08×10^{11}	–	–
Cr	MIV	1.06×10^5	1.68×10^{10}	1.06×10^5	1.68×10^{10}	–	–
Fe	SP	3.26×10^5	4.82×10^{11}	4.78×10^5	7.06×10^{11}	3.4×10^{8a}	7.5×10^{12a}
Fe	MIV	2.28×10^6	3.41×10^{11}	3.35×10^6	5.01×10^{11}	–	–
Zn	SP	4.27×10^5	2.40×10^{11}	4.27×10^5	2.36×10^{11}	–	–
Zn	MIV	8.24×10^5	1.08×10^{11}	8.24×10^5	1.08×10^{11}	–	–

Literature values cover all types of release processes as well as theoretical densities. SP densities have been calculated for the centre of the region of precipitating solar wind ions (Mura et al., 2005); PSD densities have been calculated for the sub-solar point and an orbital distance of Mercury of 0.438 AU.

[a] Killen and Ip (1999), and references therein.
[b] Sprague et al. (1993).
[c] Bida et al. (2000).
[d] Killen et al. (2005)
[e] Potter and Morgan (1997).
[f] Schleicher et al. (2004); Na is variable and the range of observed column densities is $(0.2–8.6) \times 10^{15}$ m^{-2} (Killen et al., 2007, and references therein).
[g] Killen et al. (2007) and references therein; K is variable and the range of observed column densities is $(0.5–5.5) \times 10^{13}$ m^{-2}.
[h] Kameda et al. (2009); the authors attribute their Na column densities to the impact of interplanetary dust particles on Mercury because they find a clear correlation between the Na column densities and Mercury location with respect to the ecliptic plane.
[i] Shemansky (1988).
[j] Potter et al. (2007); range over Mercury's year with good correlation of the Na column density with the true anomaly of Mercury. Extreme values of 2×10^{14} and 11.5×10^{14} atoms m^{-2} were observed as well.

sputtering or MIV. Obviously, we cannot increase the Na and K bearing minerals in the surface by two decades to match the exospheric observations since that would be in severe conflict with the mineralogical data. Potter et al. (2007) found that the Na exospheric column densities change over a Hermean year within a factor of three, and are correlated well with the true anomaly of Mercury. It has been recognised earlier that Na and K are mostly released via PSD (see review by Killen et al., 2007) or by a combined mechanism of sputtering and PSD (Mura et al., 2009). We can reproduce the observed exospheric Na and K densities when we model PSD using our elemental abundances of the surface and the PSD release process described earlier (Wurz and Lammer, 2003). For regular quiet time solar conditions we get column densities of $NC_{Na} = 3.7 \times 10^{14}$ m^{-2} and $NC_K = 1.6 \times 10^{13}$ m^{-2}, compatible with the range of observations (see Table 3). Water is also released by PSD from the surface (Westley et al., 1995) but its presence on the surface is highly unlikely, other than in permanently shadowed polar craters. Sulphur might be released by PSD if exposed to sunlight, but we do not have a cross section to quantify the process.

Shemansky (1988) reported the detection of atomic oxygen during the third Mariner 10 flyby with a density of 4.4×10^{10} m^{-3}. For sputtering we obtain an exospheric density at the surface of 2.2×10^7 m^{-3} and a column density of 4.4×10^{13} m^{-2}, which is much less than that observed. This rules out sputtering as the process to provide oxygen to the exosphere since we hardly can increase the surface abundance of oxygen, clearly not by the needed factor of about 100. We get similar results for the MIV-released oxygen (see Table 3). Alternatively, oxygen could arise from the decomposition of water in the exosphere, but the most probable process involves two steps, first $H_2O + v \rightarrow OH + H$, and second $HO + v \rightarrow O + H$ (Huebner et al., 1992). Assuming the total exospheric density of 10^{12} m^{-3}, actually an upper limit, can be attributed to water we obtain for a thermal exosphere an OH density of 1.3×10^9 m^{-3} (in good agreement with the upper limit for OH given by Killen et al., 1999) and a column density of 2.1×10^{14} m^{-2} at the sub-solar point. From this OH exosphere we get an estimate for the O exospheric density of 4×10^7 m^{-3} and a column density of 7.6×10^{11} m^{-2}. Thus thermal release cannot explain the O exosphere. Using the photon sputter rate for water of $Y_{PSD} = 3.8 \times 10^{-3}$ molecules per photon (Westley et al., 1995), we get an estimate for the H_2O exospheric density of 2.3×10^{11} m^{-3} and a column density of 1.3×10^{16} m^{-2} assuming a water mol-fraction on the surface of 1.3%. The resulting OH density at the surface is 2.5×10^8 m^{-3}, and further the resulting O density is 7.3×10^7 m^{-3} with a column density of 1.4×10^{11} m^{-2}. Thus, also PSD cannot explain the observed exospheric O density, even if we would assume a surface fully covered with water, which is highly unrealistic.

Recently, Zurbuchen et al. (2008) reported measurements of pick-up ions near Mercury and identified the mass groups Na$^+$/Mg$^+$, S$^+$/O$_2^+$, K$^+$/Ca$^+$, and others. Because of missing quantitative information in the pick-up ion spectra and the lack of species resolution it is not possible to perform a quantitative comparison between the pick-up ion measurement and our neutral densities.

One can expect that for the sputtered particles transient events in the solar wind, i.e., coronal mass ejections (CMEs), or collisions with magnetic clouds, during which the solar wind flux can increase by one to two orders of magnitude in intensity and the area of ion precipitation is enlarged as well (Kallio and Janhunen, 2003; Killen et al., 2007) will be very relevant. Thus, exospheric densities based on sputtering will be increased dramatically for the duration of the CME passage over Mercury. The duration of a CME is typically a day at Earth orbit, thus the expected duration at Mercury will be at least several hours. Potter et al. (1999) considered CMEs as an explanation for the observed Na enhancement during their observation period in November 1997.

To calculate the contribution to the exosphere by micro-meteorite impact vaporisation we start from Mercury's mass accretion rate of 10.7–23.0 tons/day, for Mercury's apocentre and pericentre, respectively (Müller et al., 2002). Earlier, Morgan et al. (1988) derived an accretion rate of 49–84 tons/day. Cintala (1992) used for the meteoritic infall on Mercury as 2.82×10^{-15} kg m^{-2} s^{-1} for meteorites with mass < 0.1 g (corresponding to a radius of < 0.02 m), which gives 0.221 kg/s or 18.2 tons/day integrated over Mercury's surface. From the mass influx we derive the fraction of volatilisation of surface material, i.e., the input into the exosphere (Cintala, 1992) from which we calculate the exospheric densities and height profiles (Wurz and Lammer, 2003). The exospheric densities we get from MIV are low (see Fig. 3, bottom panels), comparable to the densities we get from sputtering, see Table 3, with the exception that MIV operates at the entire surface and sputtering only at selected places. For Na we find a global production of exospheric Na of 2.86×10^{23} s^{-1} because of MIV, for an average micro-meteorite flux. Morgan et al. (1988) derived an average global production of 1.0×10^{23} s^{-1}, and higher values when including the contribution from the impacting meteorites. The case of MIV was also recently studied by Cremonese et al. (2005, 2006) who found that the meteorite impact results in a Na contribution to the exosphere of 1.58×10^{24} s^{-1} considering a micro-meteorite size range from 10^{-8} to 10^{-1} m radius, corresponding to Na release flux of 2.14×10^{10} s^{-1} m^{-2}. For singular impacts of larger meteorites the resulting exospheric densities can be much larger (Mangano et al., 2007). Very recently, Borin et al. (2009) reported a meteoritic flux of 2.382×10^{-14} g cm^{-2} s^{-1} that corresponds to 1540 tons/day, which is about a factor 80 higher than previous estimates mentioned above. Moreover, Kameda et al. (2009) report exospheric Na column densities in the range of $(2.5–8.5) \times 10^{-14}$ m^{-2}, which they attribute to the impact of interplanetary dust particles on Mercury because they find a clear correlation between the Na column density and Mercury being in the ecliptic plane or outside. If these Na column densities are from MIV then meteoritic fluxes as reported by Borin et al. (2009) and higher are necessary. Thus, it is possible that our estimates for the MIV contribution to the exosphere, which are based on the micro-meteorite flux from Müller et al. (2002), are too low by about two decades (see also Table 3).

One can see from our studies that the exospheric densities arising from sputtering and MIV are very low, and thus it will be an experimental challenge to measure these densities accurately, especially with in situ instrumentation from an orbiting spacecraft. In any case, sputtering, together with micro-meteorite impact vaporisation, are the only means to bring refractory elements into the exosphere.

6. Externally induced composition changes on Mercury's surface

Sputtering, PSD, and MIV change the chemical and physical state of Mercury's surface (or any planetary surface that is not protected by a sufficiently thick atmosphere). This process is known as space weathering and has been discussed in the literature extensively (e.g. Langevin 1997; Hapke 2001; Killen et al., 2007, and references therein). Here we will only discuss the changes in the elemental composition of the surface of Mercury that occur as a result of sputtering and MIV.

As one can see from the energy distribution of sputtered particles shown in Fig. 2 the sputtering process releases surface atoms (and molecules) with energies comparable to the Mercury's gravitational potential. Table 4 gives the escape fractions for particles promoted into the exosphere for sputtering, PSD (for Na and K), and for micro-meteorite impact vaporisation. Although the energy of sputtered particles is rather high, only a fraction of

Table 4
Atmospheric escape fractions for atoms released via sputtering, micrometeorite impacts, and PSD. Ionisation rates are from Huebner et al. (1992) and Killen et al. (2007).

Species	Sputtering			PSD			Micrometeorite impacts		
	$V > V_{esc}$ (%)	Ionisation (%)	Total loss (%)	$V > V_{esc}$ (%)	Ionisation (%)	Total loss (%)	$V > V_{esc}$ (%)	Ionisation (%)	Total loss (%)
O	64.1	13.2	64.6	N/A			7.70	0.44	7.90
Na	43.9	52.0	60.4	2.3	7.45	9.06	1.81	9.61	10.9
Mg	30.9	12.6	31.8	N/A			1.37	0.45	1.70
Al	61.3	88.5	92.4	N/A			0.78	36.5	36.6
Si	76.6	59.8	80.9	N/A			0.60	2.06	2.45
P	51.7	31.9	54.2	N/A			0.32	0.73	1.00
S	43.7	25.8	46.0	N/A			0.26	0.59	0.80
K	7.25	21.3	22.4	0.38	4.25	4.49	0.05	8.14	8.18
Ca	22.5	61.4	63.8	N/A			0.04	21.7	21.8
Ti	44.8	41.4	53.2	N/A			0.01	2.01	2.01
Fe	32.5	9.78	33.2	N/A			0.0	0.09	0.09
Zn	4.7	1.98	5.07	N/A			0.0	0.11	0.11

Ionisation rates for P and Ti were estimated, and are considered good within a factor of 2.

the sputtered atoms escapes the gravitational field of Mercury, some are photo-ionised and become part of the magnetosphere, and the remaining ones eventually fall back onto the surface. This is a major difference to the situation on the Moon where practically all sputtered particles escape (Wurz et al., 2007). Thus, for extended time scales there will be an elemental fractionation in Mercury's surface composition. For example, about twice as many sputtered oxygen atoms escape as sputtered iron atoms, which is a possible explanation for the nano-phase iron.

PSD is the major process to release Na and K into Mercury's exosphere, with the details of the modelling of the release process given before (Wurz and Lammer, 2003). In principle, the photo-ionisation times for Na and K at Mercury are short (for Na they range from 5840 to 13,450 s from pericentre to apocentre, respectively; Huebner et al., 1992), but during the moderately short ballistic flight times resulting from the PSD process only a small fraction of Na and K atoms are ionised (see Table 4). Most of the desorbed Na and K atoms thus fall back onto the surface. Since PSD is a highly selective release process, affecting only Na and K, but leaving the majority of atoms on the surface, the lost Na and K atoms have to be replenished on the surface. Killen et al. (2005) studied the supply of Na to the surface by thermal diffusion through regolith grains and found that a maximum Na flux to the surface of 10^{11} atoms m^{-2} s^{-1} can be maintained, which is considerably lower than the Na flux of 2.1×10^{12} atoms m^{-2} s^{-1} we need to compensate for the exospheric Na losses (see Table 4). Thus, more energetic processes have to be responsible for providing the Na on the surface, as was already concluded by Killen et al. (2005). Moreover, since the Na content in the exosphere is relatively constant over Mercury's year (within a factor of 2; Potter et al., 2007) these energetic processes have to be active continuously, and not be of an episodic nature. Mura et al. (2009) showed that chemical changes on the surface introduced by ion impact can account for the observed Na exosphere.

For micro-meteorite impact vaporisation only light elements escape since the impact produced cloud is described by a thermal distribution with a temperature of 4000 K (Wurz and Lammer, 2003). From the non-volatile material released by MIV, a small fraction escape the gravity field, notably oxygen escapes and the heavier atoms at progressively smaller fractions. Again, there is a preferential loss of oxygen from the surface. Thus both sputtering and MIV tend to chemically reduce the surface and increase the metallic content.

In addition to the loss of atoms from the exosphere promoted into the exosphere by sputtering and by MIV, ionisation of these exospheric species plays an additional role as a loss process from Mercury's exosphere because the ions are picked up by the electromagnetic fields of Mercury's magnetosphere to become part of the magnetospheric ion population. The fraction of ionised atoms in the exosphere is also given in Table 4 for particle release via sputtering, MIV, and PSD, together with the total loss fractions. Depending on species, exospheric losses because of photo-ionisation can be significant. Photo-ionisation is calculated using the photo-ionisation rates for quiet Sun (Huebner et al., 1992; Killen et al., 2007) prorated to Mercury's orbit. The ionised particles will immediately become part of Mercury's magnetosphere with the possibility to return to the surface (Delcourt et al., 2003; Kallio and Janhunen, 2003). Depending on their energy these ions may either be adsorbed on the surface or implanted at larger depth. For Ar ions with energies ≥ 3 keV almost 100% are known to be trapped in the lunar grains (Bühler et al., 1966; Manka and Michel, 1970). In addition, these ions can also cause sputtering of surface material. A detailed study that will investigate the role of heavy exospheric ions to surface sputtering is beyond the scope of this work but is considered for the future.

Large fractions of Mercury's surface are protected from the solar wind by Mercury's magnetosphere. Typically an area of about 3×10^{12}–2×10^{13} m^2 (Killen et al., 2007, and references therein) at the Sun-facing surface is bombarded by solar wind ions resulting in a total flux of solar wind ions of about 1.5×10^{12}–2×10^{13} ions m^{-2} s^{-1} onto the exposed surface (Killen et al., 2007, and references therein), which is variable with time. This ion flux corresponds to 2.5×10^{-15}–3.3×10^{-14} kg m^{-2} s^{-1}. Integrated over the exposed surface we get a total of 3×10^{25} ions s^{-1} on average (Killen et al., 2007, and references therein), which corresponds to 0.05 kg s^{-1}. In comparison, the meteoritic infall on Mercury is much larger, as discussed above. The influx of solar material is much smaller than the meteoritic influx, and even less is the ion flux onto the surface in the auroral precipitation bands. Therefore, we do not have to worry about a possible composition change of the top-most surface by deposition (implantation) of solar material since that will be masked by composition changes from meteoritic infall. The infall of meteorites will have contaminated the Hermean surface over the billions of years of meteoritic bombardment. By comparing to the Moon it has been estimated that 5–20% of Mercury's regolith is of meteoritic origin (Cintala, 1992).

7. Conclusion

We have extended our Monte-Carlo model of exospheres (Wurz and Lammer, 2003) to calculate the exospheric contributions from the ion-induced sputtering process, photon-stimulated desorption, and micro-meteorite impact vaporisation in a self-consistent way

based on a global model of the mineralogical composition of the surface. This extended Monte-Carlo model will be used as a tool to investigate expected exospheric abundances in support of the in situ measurements of exospheric species by the SERENA instrument on BepiColombo mission (Orsini et al., 2010).

Based on available literature data for the mineralogical and exospheric composition of Mercury, we established a global model for the surface mineralogy and from that derived the average elemental composition of the surface. The optical observations (visible and IR) as well as the exosphere composition reflect Mercury's top-most surface that has undergone space weathering over millions of years. Thus, our mineralogical model reflects the present space-weathered surface. Our mineralogical model is based on end-member minerals, rather than particular minerals suggested in the literature to establish a general global modal mineralogical model for Mercury's surface. We compared the results obtained from the simple additive composition modelling method with a complex but more realistic multiplicative approach and found that the subcomposition formed by the trace elements in some minerals are near the barycenter of the simplex space geometry (used in the multiplicative method compared to the Euclidian space geometry of the additive method) so that both methods produce comparable results. Therefore, one can conclude that in that particular case the additive method yields also accurate results.

From Mariner 10 observations an upper limit for total exospheric density of 10^{12} m^{-3} at the surface was established. We find that the contribution to the exosphere density at the surface by sputtering is only about $4-10^7$ m^{-3}, and by MIV it is about 1.6×10^8 m^{-3}. However, exospheric densities from MIV are more uncertain because of the uncertainties in the meteoritic accretion rates of Mercury, and could be even a factor of 100 higher. In conclusion, sputtering and micro-meteorite impact vaporisation contribute only a small fraction of Mercury's exosphere, at least close to the surface. Because of the considerably larger scale height of atoms released via sputtering into the exosphere, sputtered atoms start to dominate the exosphere at altitudes exceeding around 1000 km, with the exception of some light and abundant species released thermally, e.g. H_2 and He, with the constraint that H_2 has not been observed yet, but has been postulated to exist at these amounts (Killen and Ip, 1999).

Because of Mercury's strong gravity field not all particles released by sputtering and micro-meteorite impact can escape. As well as losses by ionisation, the significance of which varies for different elements, there are considerable differences in the total loss, notably much more oxygen is lost than iron. Over extended time scales these differences in exospheric loss will lead to an alteration of the surface composition. This is in contrast to the Moon, where the exospheric loss is similar for all elements (Wurz et al., 2007). Thus, Mercury is unique in terms of space weathering of its surface because of its large gravity compared to the Moon.

Appendix A

To compare the traditional additive procedure and the multiplicative perturbation mechanism for producing intermediates compositions used in composition modelling we consider a simple situation: two scientists, SC1 and SC2 are dealing with the process of change from chemical composition of rock R to soil S. Technical instruments of scientist SC1 allow to measure all (three) chemical elements from both R and S. Therefore he works with the full compositions $R=(R1, R2, R3)$ and $S=(S1, S2, S3)$. On the other hand, technical instruments of scientist SC2 only allow measurements of the two first chemical elements. Then, he works with subcompositions from R and S. Both scientists are interested in to estimate the relation between the two first chemical elements when the change process from R to S is in an intermediate composition. The subcompositional coherence principle implies that the estimates of both scientists must be the same.

For illustrating the situation we consider a simple specific case: the scientist SC1 has measured the full compositions $R=(0.2, 0.1, 0.7)$ and $S=(0.4, 0.3, 0.3)$. The second scientist SC2 has measured the corresponding subcompositions in relation to the two first chemical elements: $R_{12}=(2/3, 1/3)$ and $S_{12}=(4/7, 3/7)$. Note that these subcompositions are obtained from the full compositions R and S, taking the two first elements and closing them to 1.

To calculate any intermediate composition between the rock and the soil, the scientist can apply the traditional procedure or can apply the perturbation mechanism. When the traditional procedure is applied, the intermediate composition is produced using the formula:

$$\alpha R + (1-\alpha)S, \quad \text{for } 0 \leq \alpha \leq 1. \tag{A1}$$

For calculating the intermediate composition by the perturbation mechanism the formula given by Eq. (5) should be applied. Table (A1) shows the intermediate compositions for $\alpha=0.5$, that is the central intermediate between the rock and the soil. Note that for $\alpha=0.5$, the traditional procedure produces the arithmetic mean from the compositions. Instead, the perturbation mechanism procedure deals with the geometric mean. Results from Table A1 indicate that using the perturbation mechanism procedure the principle of subcompositional coherence is guaranteed. Both

Table A1
Intermediate subcompositions calculated by both procedures and scientists for the same $\alpha=0.5$ value.

Additive method "traditional procedure"		
First scientist SC1: $R=(0.2, 0.1, 0.7)$, $S=(0.4, 0.3, 0.3)$	Intermediate subcomposition	(0.6, 0.4)
Intermediate full composition ⟨0.3, 0.2, 0.50⟩		
Second scientist SC2: $R_{12}=(2/3, 1/3)$, $S_{12}=(4/7, 3/7)$	Intermediate subcomposition	(0.619, 0.381)
Multiplicative "perturbation mechanism procedure" (Eq. 5)		
First scientist: $R=(0.2, 0.1, 0.7)$, $S=(0.4, 0.3, 0.3)$	Intermediate subcomposition	(0.6202, 0.3798)
Intermediate full composition ⟨0.3094, 0.1894, 0.5012⟩		
Second scientist: $R_{12}=(2/3, 1/3)$, $S_{12}=(4/7, 3/7)$	Intermediate subcomposition	(0.6202, 0.3798)

scientists produce exactly the same intermediate subcomposition (0.6202, 0.3798). That is the relation between the two chemical elements is $0.3798/0.6202=61.24\%$. On the contrary the traditional or additive procedure for calculating the intermediates does not verify this principle. The scientist SC1 obtains (0.6, 0.4) and concludes that the relation between the two first chemical elements is $0.4/0.6=66.67\%$. Instead, the scientist SC2 respectively obtains (0.619, 0.381) and $0.381/0.619=61.55\%$. That is, they use the same information but obtain different conclusions. The principle of subcompositional coherence is violated.

Appendix B

Ions hitting a solid surface will cause the release of surface atoms because of the deposition of kinetic energy. This process is called sputtering, and occurs on all objects in the solar system that are not protected by an atmosphere because of the solar wind. The solar wind consist of protons (about 95%), alpha particles (about 5%), and heavy ions ($<0.1\%$) (see review by Wurz, 2005, and references therein). The heavy ions in the solar wind are multiply charged because of the million-degree hot solar corona. Oxygen, for example, is present in the solar wind with charge states of typically +6 and +7; iron is present with charge states typically in the range from +8 to +12 (Aellig et al., 1999a, 1999b). These high charge states mean that the ions have high internal energies (potential energies), for example, 295 eV for O^{6+} and 1055 eV for Fe^{10+}, as compared to singly or doubly charged ions. However, these high internal energies (potential energies) have to be compared to their kinetic energies in the solar wind ions of typically 16 keV for oxygen ions and 56 keV for iron ions for a solar wind speed of 440 km/s. It has been argued that the sputter yield for heavy ions of the solar wind impacting on a planetary surface is increased by a factor of 10–1000 as a result of their high internal energy resulting from their high charge state (Shemansky, 2003), based on laboratory measurements (e.g. Hayderer et al., 2001).

The charge state of an impacting ion affects the sputtering yield due to its available potential (ionisation) energy, hence the term "potential sputtering" (Aumayr and Winter, 2004). There is a considerably large body of laboratory research on the interaction of multiply charged ions with solid surfaces, which has been reviewed recently for multiply charged ions (Arnau et al., 1997; Aumayr and Winter, 2004), and for highly charged ions (Schenkel et al., 1999). In the following we will briefly summarise these findings.

For metallic surfaces and semiconductors (Si and GaAs) no deviation of the sputter yield for highly charged ions from the sputter yield of singly charged ions was found, with the highest charge states investigated being Ar^{9+} and Xe^{25+}. Moreover, all the measured sputter yields agree with the TRIM calculations, a software package which considers only the kinetic energy of the impacting ions (Ziegler et al., 1984).

For ionic crystals (NaCl and LiF) a pronounced increase with ionic charge state was observed; for NaCl the sputter yield increased by a factor of 4 for Ar^{8+} ions compared to Ar^{+} ions, for LiF the sputter yield increased by a factor of 25 for Ar^{14+} ions compared to Ar^{+} ions. Note that Ar charge states in the solar wind range from +8 to +11. For oxides, which are the best analogue for Mercury's surface, a clear signature of a sputter yield increase for highly charged ions was observed for SiO_2, Al_2O_3, and MgO. For SiO_2 this increase was about 3 for Ar^{8+} ions compared to Ar^{+} ions, and about 65 for Xe^{25+} ions compared to Ar^{+} ions. Similar enhancements were found for the Al_2O_3 surface. For MgO the sputter yield increased by a factor of 6 for Ar^{14+} ions compared to Ar^{+} ions. Measured sputter yields of 1.5 keV Xe^{q+} onto Al_2O_3

show an approximately 40-fold increase in the sputter yield for Xe^{28+} over that of Xe^{9+}. Both of these materials appear to have a finite sputter yield at zero kinetic energy of the projectile. On the other hand, for a highly ionic oxide such as MgO, even though potential energy greatly increases the sputter yield, potential energy does not induce sputtering in the absence of kinetic energy of the projectile.

Moreover, the enhancement of the sputter yield is strongly depending on the ion dose the surface has been exposed to. After a removal of about a monolayer from the oxide surface the sputter yield for highly charged ions drops to about the values for singly charged ions. Removal of a monolayer of surface material corresponds to a heavy ion flux of a few 10^{13} ions $cm^{-2}\,s^{-1}$ at solar wind energies, which takes about two weeks at Mercury's orbit. This reduction in sputter yield is attributed to the very surface becoming reasonably conductive (by preferential loss of oxygen and the creation crystal defects) and thus the highly charged ions become decharged; that is, they lose their internal energy when they approach the surface.

Appendix C

Particle sputtering: the sputter yield for particles sputtered from a solid is given by the total sputter yield Y_{tot} and the normalised energy distribution $f(E_e)$, with the energy E_e, and normalised angular distribution $f(\alpha)$, with α the polar angle of the emitted particle:

$$Y(E_e,\alpha) = Y_{tot} f(E_e) f(\alpha) \tag{C1}$$

There is no azimuth angle dependence considered. The energy distribution of the sputtered particle, has been given as (Sigmund, 1969):

$$f(E_e) = \frac{6E_b}{3-8\sqrt{E_b/E_c}} \frac{E_e}{(E_e+E_b)^3}\left\{1-\sqrt{\frac{E_e+E_b}{E_c}}\right\}, \tag{C2}$$

where E_b is the surface binding energy of the sputtered particle and E_c is the cut-off energy. The cut-off energy is the maximum energy that can be imparted to a sputtered particle by a projectile particle with energy E_i. It is given by the limit imposed by a binary collision between a projectile atom M_1 and the target atom M_2 (to be sputtered) as

$$E_c = E_i \frac{4M_1 M_2}{(M_1+M_2)^2}. \tag{C3}$$

Fig. 2 shows examples of the energy distribution for typical atoms sputtered from Mercury's surface under solar wind bombardment. Note that the maximum of the energy distribution (C2) is at $E_{max}=E_b/2$, with E_b the binding energy of the atom at the surface. The values of E_b used in the calculation are given in Table C1. At higher energies the distribution falls off with E_e^{-2}, which was observed experimentally earlier (e.g., Thompson et al., 1968; Husinsky et al., 1985). Note that if the energy of the incident ion is so low that the cut-off energy E_c approaches the binding energy, the energy distribution of sputtered atoms becomes rather narrow.

Table C1
Surface binging energies in [eV] as used in the calculation of the energy distribution of sputtered atoms (in Eq. (C2)).

O	Na	Mg	Al	Si	P	S	K	Ca	Ti	Cr	Fe	Zn	OH
2.0	2.0	1.54	3.36	4.7	3.27	2.88	0.93	2.1	4.89	4.12	4.34	1.35	1.50

The average release velocity is derived from the sputter distribution (see Eq. (C2) and Fig. 2) as

$$\langle v_i \rangle = \frac{\int v f(v) dv}{\int f(v) dv} = \frac{1}{2} v_1^2 v_2 \left(-\frac{3v_1^2 + 5v_2^2}{(v_1^2 + v_2^2)^2} + \frac{3 \arctan(v_2/v_1)}{v_1 v_2} \right) \quad \text{(C3)}$$

with the abbreviations

$$v_1 = \sqrt{\frac{2E_b}{m_2}} \quad \text{and} \quad v_2 = \frac{4v_{SW}}{M_1 + M_2}$$

where E_b is the binding energy of species i in the particular chemical mix of the surface, m_2 is the mass of the sputtered atom in kg, and M_1 and M_2 are the atomic numbers for the incoming and the sputtered atom, respectively. Note that the most probable velocity is $v_{mp} = \sqrt{E_{b,i}/m_2}$, which is lower.

The polar angle distribution of sputtered atoms, $f(\alpha)$, for polycrystalline surfaces is best described by a quadratic angular dependence, $f(\alpha) \propto \cos^2 \alpha$ for laboratory experiments (Hofer, 1991). However, Cassidy and Johnson (2005) found that for the fine-grained and porous regolith a better choice is $f(\alpha) = \cos \alpha$, which is used in our calculations.

Photon stimulated desorption: the flux of particles released by photon stimulated desorption (PSD) is given by Yakshinskiy and Madey (1999):

$$\Phi_{PSD}(E_e, \alpha) \approx \tfrac{1}{4} f_{PSD}(E_e) f_\alpha C_i \phi_{ph} Q_i, \quad \text{(C4)}$$

where C_i is surface concentration of species i, ϕ_{ph} is the solar photon flux in the UV wavelength range at the distance of Mercury, and Q_i is the cross section for PSD. Q_i is species specific and we used for sodium $Q_{Na} = 3.0 \times 10^{-24}$ m^2 (Yakshinskiy and Madey, 1999), potassium $Q_K = 2.0 \times 10^{-24}$ m^2 from Madey et al. (1998), and water $Q_{H_2O} = 1.0 \times 10^{-22}$ m^2 adapted from Westley et al. (1995). The energy distribution, $f_{PSD}(E_e)$, is based on the distribution given by Johnson et al. (2002), but extended by an energy cut-off and normalised:

$$f_{PSD}(E_e) = \frac{E_{max}(1-\beta^2)\beta}{E_{max}(1-\beta) + U(1+\beta)} \frac{E_e U^\beta}{(E_e + U)^{2+\beta}} \left(1 - \frac{E_e + U}{E_{max}} \right), \quad \text{(C5)}$$

where U is the characteristic energy of particles released by PSD, β is the shape parameter of the distribution, and E_{max} is the maximum energy a released particle can have. For the shape parameter we used the values $\beta_{Na} = 0.7$ and $\beta_K = 0.25$ from Johnson et al. (2002) and $\beta_{H_2O} = 0.7$ (estimate). The characteristic energy is related to the surface temperature by

$$U = \frac{k_B T_0}{e} \quad \text{in [eV] with} \quad T_0 = T_i + T_S(\phi, \varphi), \quad \text{(C6)}$$

where k_B is the Boltzmann constant, e is the elementary charge, and T_S is the local surface temperature. T_i is species specific and we used for sodium $T_{Na} = 600$ K and for potassium $T_K = 400$ K based on Killen et al. (1999), and water $T_{H_2O} = 0$ K. Based on the solar XUV spectrum we chose an upper limit of $E_{max} = 20$ eV. The energy distribution has its maximum at $E_e = U/(1+\beta)$. The dependence on the polar angle of particle release is $f(\alpha) = \cos \alpha$, and there is no azimuth angle dependence considered.

Meteoritic impact vaporisation: MIV is modelled as thermal evaporation using a temperature of 4000 K (see Wurz and Lammer, 2003). Fluxes of impacting meteoritic material on Mercury's surface are converted to released fluxes of volatiles based on the work by Cintala (1992).

References

Aellig, M.R., Hefti, S., Grünwaldt, H., Bochsler, P., Wurz, P., Ipavich, F.M., Hovestadt, D., 1999a. The Fe/O elemental abundance ratio in the solar wind as observed with SOHO/CELIAS/CTOF. J. Geophys. Res. 104 (A11), 24769–24780.

Aellig, M.R., Bochsler, P., Grünwaldt, H., Hefti, S., Wurz, P., Hilchenbach, M., Hovestadt, D., Ipavich, F.M., Gliem, F., 1999b. The influence of suprathermal electrons on the derivation of the coronal electron temperatures from solar wind minor ion charge states. Phys. Chem. Earth (C) 24 (4), 407–414.

Aitchison, J., 1986. The Statistical Analysis of Compositional Data. Chapman & Hall, London. Reprinted in 2003 by The Blackburn Press, Caldwell, New York.

Aitchison, J., Barceló-Vidal, C., 2002. Compositional processes: a statistical search for understanding. In: Terra Nostra, Proceedings of IAMG'02 Eighth Annual Conference of the International Association for Mathematical Geology, Germany, Berlin, vol. 3, pp. 381–383.

Arnau, A., Aumayr, F., Echenique, P.M., Grether, M., Heiland, W., Limburg, J., Morgenstern, R., Roncin, P., Schippers, S., Schuch, R., Stolterfoht, N., Varga, P., Zouros, T.J.M., Winter, H.P., 1997. Interaction of slow multicharged ions with solid surfaces. Surf. Sci. Rep. 27, 113–239.

Aumayr, F., Winter, H., 2004. Potential sputtering. Philos. Trans. R. Soc. Lond. A 362, 77–102.

Betz, G., Wehner, G.K., 1983. Sputtering of multicomponent materials. In: Berisch, R. (Ed.), Sputtering by Particle Bombardment II. Springer-Verlag, New York, pp. 11–90.

Bida, T.A., Killen, R.M., Morgan, T.H., 2000. Discovery of calcium in Mercury's atmosphere. Nature 404, 159–161.

Biersack, J.P., Eckstein, W., 1984. Sputtering of solids with the Monte Carlo program TRIM.SP. Appl. Phys. A 34, 73–94.

Blewett, D.T., Lucey, P.G., Hawke, B.R., Ling, G.G., Robinson, M.S., 1997. A comparison of Mercurian reflectance and spectral quantities with those of the Moon. Icarus 129, 217–231.

Blewett, D.T., Hawke, B.R., Lucey, P.G., 2002. Lunar anorthosite as a spectral analog for Mercury. Meteorit. Planet. Sci. 37, 1245–1254.

Borin, P., Cremonese, G., Marzari, F., Bruno, M., Marchi, S., 2009. Statistical analysis of micrometeoroids flux on Mercury. Astron. Astrophys. 503, 259–264.

Broadfoot, A.L., Shemansky, D.E., Kumar, S., 1976. Mariner 10: Mercury atmosphere. Geophys. Res. Lett. 3, 577–580.

Bühler, F., Geiss, J., Meister, J., Eberhardt, P., Huneke, J.C., Signer, P., 1966. Trapping of the solar wind in solids—I. Earth Planet. Sci. Lett. 1, 249–255.

Burbine, T.H., McCoy, T.J., Nittler, L.R., Benedix, G.K., Cloutis, E.A., Dickinson, T.L., 2002. Spectra of extremely reduced assemblages: implications for Mercury. Meteor. Plan. Sci. 37, 1233–1244.

Cassidy, W., Johnson, R.E., 2005. Monte Carlo model of sputtering and other ejection processes within a regolith. Icarus 176, 499–507.

Cintala, M.J., 1992. Impact-induced thermal effects in the lunar and Mercurian regoliths. J. Geophys. Res. 97, 947–973.

Cremonese, G., Bruno, M., Mangano, V., Marchi, S., Milillo, A., 2005. Release of neutral sodium from the surface of Mercury induced by meteorid impacts. Icarus 177, 122–128.

Cremonese, G., Bruno, M., Mangano, V., Marchi, S., Milillo, A., 2006. Corrigendum to "Release of neutral sodium atoms from the surface of Mercury induced by meteroid impacts" (Icarus 177 (2005) 122–128). Icarus 182, 297–298.

Delcourt, D.C., Grimald, S., Leblanc, F., Berthelier, J.-J., Millilo, A., Mura, A., Orsini, S., Moore, T.E., 2003. A quantitative model of the planetary Na$^+$ contribution to Mercury's magnetosphere. Ann. Geophys. 21, 1723–1736.

Denevi, B.W., Robinson, M.S., Solomon, S.C., Murchie, S.L., Blewett, D.T., Dominiqu, D.L., McCoy, T.J., Ernst, C.M., Head, J.W., Watters, T.R., Chabot, N.L., 2009. The evolution of Mercury's crust: a global perspective from MESSENGER. Science 324, 613–618.

Emery, J.P., Sprague, A.L., Witteborn, F.C., Colwell, J.E., Kozlowski, R.W.H., Wooden, D.H., 1998. Mercury: thermal modelling and mid-infrared (5–12 μm) observations. Icarus 136, 104–123.

Fegley Jr., B., Cameron, A.G.W., 1987. A vaporization model for iron/silicate fractionation in the Mercury protoplanet. Earth Planet. Sci. 82, 207–222.

Fjeldbo, G., Kliore, A., Sweetnam, D., Esposito, P., Seidel, B., Howard, T., 1976. The occultation of Mariner 10 by Mercury. Icarus 29, 407–415.

Goettel, K.A., 1988. Present bounds on the bulk composition of Mercury: implications for planetary formation processes. In: Vilas, F., Chapman, C.R., Matthews, M.S. (Eds.), Mercury, University of Arizona Press, Tucson, p. 613.

Hapke, B., 2001. Space weathering from Mercury to the asteroid belt. J. Geophys. Res. 106 (E5), 10039–10074.

Harmon, J.K., Slade, M.A., 1992. Radar mapping of Mercury—full-disk images and polar anomalies. Science 258, 640–643.

Hayderer, G.S., Cernusca, S., Schmid, M., Varga, P., Winter, HP., Aumayr, F., Niemann, D., Hoffmann, V., Stolterfoht, N., Lemell, C., Wirtz, L., Burgdörfer, J., 2001. Kinetically assisted potential sputtering of insulators by highly charged ions. Phys. Rev. Lett. 86, 3530–3533.

Hofer, W.O., 1991. Angular, energy, and mass distribution of sputtered particles. In: Behrisch, R., Wittmaack, K. (Eds.), Sputtering by Particle Bombardment, pp. 15–90.

Huebner, W.F., Keady, J.J., Lyon, S.P., 1992. Solar photo rates for planetary atmospheres and atmospheric pollutants. Astrophys. Space Sci. 195, 1–294.

Hunten, D.M., Morgan, T.H., Shemansky, D., 1988. The Mercury atmosphere. In: Vilas, F., Chapman, C.R., Matthews, M.S. (Eds.), Mercury. University of Arizona Press, Tucson, pp. 562.

Husinsky, W., Girgis, I., Betz, G., 1985. Doppler shift laser fluorescence spectroscopy of sputtered and evaporated atoms under Ar$^+$ bombardment. J. Vac. Sci. Technol. B 3 (5), 1543–1545.

Johnson, R.E., Leblanc, F., Yakshinskiy, B.V., Madey, T.E., 2002. Energy distributions for desorption of sodium and potassium from ice: the Na/K ratio at Europa. Icarus 156, 136–142.

Kabin, K., Gombosi, T.I., DeZeeuw, D.L., Powell, K.G., 2000. Interaction of Mercury with the solar wind. Icarus 143, 397–406.

Kallio, E., Janhunen, P., 2003. Solar wind and magnetospheric ion impact on Mercury's surface. Geophys. Res. Lett., 30. doi:10.1029/2003GL017842.

Kameda, S., Yoshikawa, I., Ono, J., Nozawa, H., 2007. Time variation in exospheric sodium density on Mercury. Planet. Space Sci. 55 (11), 1509–1517.

Kameda, S., Yoshikawa, I., Kagitani, M., Okano, S., 2009. Interplanetary dust distribution and temporal variability of Mercury's atmospheric Na. Geophys. Res. Lett. 36, L15201. doi:10.1029/2009GL039036.

Kerber, L., Head, J.W., Solomon, S.C., Murchie, S.L., Blewett, D.T., Wildon, L., 2009. Explosive volcanic eruptions on Mercury: eruption conditions, magma volatile content and implications for interior volatile abundances. Earth Planet. Sci. Lett. 285, 263–271.

Killen, R.M., Potter, A.E., Morgan, T.H., 1990. Spatial distribution of sodium vapor in the atmosphere of Mercury. Icarus 85, 145–167.

Killen, R.M., Potter, A., Fitzsimmons, A., Morgan, T.H., 1999. Sodium D2 line profiles: clues to the temperature structure of Mercury's exosphere. Planet. Space Sci. 47, 1449–1458.

Killen, R.M., Ip, W.-H., 1999. The surface-bounded atmospheres of Mercury and the Moon. Rev. Geophys. 37 (3), 361–406.

Killen, R.M., Bida, T.H., Morgan, T.H., 2005. The calcium exosphere of Mercury. Icarus 173, 300–311.

Killen, R., Cremonese, G., Lammer, H., Orsini, S., Potter, A.E., Sprague, A.L., Wurz, P., Khodachenko, M.L., Lichtenegger, H.I.M., Milillo, A., Mura, A., 2007. Processes that promote and deplete the exosphere of Mercury. Space Sci. Rev. 132, 433–509.

Kolb, C., Martín-Fernández, J.A., Abart, R., Lammer, H., 2006. The chemical variability at the surface of Mars. Icarus 183 (1), 10–29.

Lammer, H., Wurz, P., Patel, M.R., Killen, R., Kolb, C., Massetti, S., Orsini, S., Milillo, A., 2003. The variability of Mercury's exosphere by particle and radiation induced surface release processes. Icarus 166, 238–247.

Langevin, Y., 1997. The regolith of Mercury: present knowledge and implications for the Mercury Orbiter. Planet. Space Sci. 45, 31–38.

Leblanc, F., Delcourt, D., Johnson, R.E., 2003. Mercury's sodium exosphere: magnetospheric ion recycling. J. Geophys. Res. 108, 5136. doi:10.1029/2003JE002151.

Leblanc, F., Doressoundiram, A., Schneider, N., Massetti, S., Wedlund, M., López Ariste, A., Barbieri, C., Mangano, V., Cremonese, G., 2009. Short-term variations of Mercury's Na exosphere observed with very high spectral resolution. Geophys. Res. Lett. 36, L07201. doi:10.1029/2009GL038089.

Madey, T.E., Yakshinskiy, B.V., Ageev, V.N., Johnson, R.E., 1998. Desorption of alkali atoms and ions from oxide surfaces: relevance to origins of Na and K in atmospheres of Mercury and the Moon. J. Geophys. Res. 103, 5873–5887.

Mangano, V., Milillo, A., Mura, A., Orsini, S., DeAngelis, E., DiLellis, A.M., Wurz, P., 2007. The contribution of impact-generated vapour to the Hermean atmosphere. Planet. Space Sci. 55 (11), 1541–1556.

Manka, R.H., Michel, F.C., 1970. Lunar atmosphere as a source of Argon-40 and other lunar surface elements. Science 169, 278–280.

Martín-Fernández J.A., Bren, M., 2001. Some practical aspects on multidimensional scaling of compositional data. In: Proceedings of the Annual Conference of the International Association for Mathematical Geology, Cancun (Mexico), CD-ROM, p. 16.

Martín-Fernández, J.A., Barceló-Vidal, C., Pawlowsky-Glahn, V., 2003. Dealing with zeros and missing values in compositional data sets. Math. Geol. 35, 253–278.

Martín-Fernández, J.A., Thió-Henestrosa, S., 2006. Rounded zeros: some practical aspects for compositional data. Compositional Data Analysis in the Geosciences: from Theory to Practice. Geological Society, London, Special Publications, vol. 264, pp. 191–201.

Massetti, S., Orsini, S., Milillo, A., Mura, A., DeAngelis, E., Lammer, H., Wurz, P., 2003. Mapping of the cusp plasma precipitation on the surface of Mercury. Icarus 166, 229–237.

McClintock, W.E., Bradley, E.T., Vervack, R.J., Killen, R.M., Sprague, A.L., Izenberg, N.R., Solomon, S.C., 2008a. Mercury's exosphere: observations during MESSENGER's first Mercury flyby. Science 321, 92–95.

McClintock, W.E., Izenberg, N.R., Holsclaw, G.M., Blewett, D.T., Domingue, D.L., Head III, J.W., Helbert, J., McCoy, T.J., Murchie, S.L., Robinson, M.S., Solomon, S.C., Sprague, A.L., Vilas, F., 2008b. Spectroscopic observations of mercury's surface reflectance during MESSENGER's first Mercury Flyby. Science 321, 62–65.

McClintock, W.E., Vervack, R.J., Bradley, E.T., Killen, R.M., Mouawad, N., Sprague, A.L., Burger, M.H., Solomon, S.C., Izenberg, N.R., 2009. MESSENGER observations of Mercury's exosphere: detection of magnesium and distribution of constituents. Science 324, 610–613.

McCubbin, F.M., Steele, A., Hauri, E.H., Nekvasil, H., Yamashita, S., Hemley, R.J., Nominally hydrous magmatism on the Moon. Proc. Natl. Acad. Sci., in press, doi:10.1073/pnas.1006677107.

Milillo, A., Wurz, P., Orsini, S., Delcourt, D., Kallio, E., Killen, R.M., Lammer, H., Massetti, S., Mura, A., Barabash, S., Cremonese, G., Daglis, I.E., DeAngelis, E., Di Lellis, A.M., Livi, S., Mangano, V., Torkar, K., 2005. Surface–exosphere–magnetosphere system of Mercury. Space Sci. Rev. 117, 397–443.

Milillo, A., Fujimoto, M., Kallio, E., Kameda, S., Leblanc, F., Narita, Y., Cremonese, G., Laakso, H., Laurenza, M., Massetti, S., McKenna-Lawlor, S., Mura, A., Nakamura, R., Omura, Y., Rothery, D.A., Seki, K., Storini, M., Wurz, P., Baumjohann, W., Bunce, E., Kasaba, Y., Helbert, J., Sprague, A., 2010. The BepiColombo mission: an outstanding tool for investigating the Hermean environment. Planet. Space Sci. 58, 40–60.

Mitchell, D., de Pater, I., 1994. Microwave imaging of Mercury's thermal emission at wavelengths from 0.3 to 20.5 cm. Icarus 110, 2–32.

Morgan, J.W., Anders, E., 1980. Chemical composition of Earth, Venus, and Mercury. Proc. Natl. Acad. Sci. USA 77, 6973–6977.

Morgan, T.H., Zook, H.A., Potter, A.E., 1988. Impact-driven supply of sodium and potassium to the atmosphere of Mercury. Icarus 75, 156–170.

Müller, M., Green, S.F., McBride, N., Koschny, D., Zarnecki, J.C., Bentley, M.S., 2002. Estimation of the dust flux near Mercury. Planet. Space Sci. 50, 1101–1115.

Mura, A., Orsini, S., Milillo, A., Delcourt, D., Massetti, S., DeAngelis, E., 2005. Dayside H+ circulation at Mercury and neutral particle emission. Icarus 175, 305–319.

Mura, A., Wurz, P., Lichtenegger, H.I.M., Lammer, H., Milillo, A., Schleicher, H., Massetti, S., Orsini, S., 2009. The sodium exosphere of Mercury: comparison between observations during Mercury's transit and model results. Icarus 200, 1–11.

Orsini, S., Livi, S., Torkar, K., Barabash, S., Milillo, A., Wurz, P., Di Lellis, A.M., Kallio, E., 2010. and the SERENA team, 2010. SERENA: a suite of four instruments (ELENA, STROFIO, PICAM and MIPA) on board BepiColombo-MPO for particle detection in the Hermean environment. Planet. Space Sci. Planet. Space Sci. 58, 166–181.

Potter, A.E., 1995. Chemical sputtering could produce sodium vapour and ice on Mercury. Geophys. Res. Lett. 22, 3289–3292.

Potter, A.E., Morgan, T.H., 1985. Discovery of sodium in the atmosphere of Mercury. Science 229, 651–653.

Potter, A.E., Morgan, T.H., 1986. Potassium in the atmosphere of Mercury. Icarus 67, 336–340.

Potter, A.E., Morgan, T., 1990. Evidence for magnetospheric effects on the sodium atmosphere of Mercury. Science 248, 835–838.

Potter, A.E., Morgan, T.H., 1997. Evidence for suprathermal sodium on Mercury. Adv. Space Res. 19, 1571–1576.

Potter, A.E., Killen, R.M., Morgan, T.H., 1999. Rapid changes in the sodium exosphere of Mercury. Planet. Space Sci. 47, 1441–1448.

Potter, A.E., Anderson, C.M., Killen, R.M., Morgan, T.H., 2002. Ratio of sodium to potassium in the Mercury exosphere. J. Geophys. Res. 107 (E6. doi:10.1029/2000JE001493.

Potter, A.E., Killen, R.M., Morgan, T.H., 2007. Solar radiation acceleration effects on Mercury sodium emission. Icarus 186 (2), 571–580.

Rothery, D.A., Marinangli, L., Anand, M., Carpenter, J., Christensen, U., De Santis, M.C., Epifani, E.M., Erard, S., Frigeri, A., Fraser, G., Haubner, E., Helbert, J., Hiesinger, H., Joy, K., Langevin, Y., Massironi, M., Milillo, A., Mitrifanov, I., Muinonen, K., Näränen, J., Pauselli, C., Potts, P., Wurz, P., 2010. Mercury's surface and composition studied by BepiColombo. Planet. Space Sci. 58, 21–39.

Sarantos, M., Reiff, P.H., Hill, T.W., Killen, R.M., Urquhart, A.L., 2001. A Bx-interconnected magnetosphere model for Mercury. Planet. Space Sci. 49, 1629–1635.

Schenkel, T., Hamza, A.V., Barnes, A.V., Schneider, D.H., 1999. Interaction of slow, very highly charged ions with surfaces. Progr. Surf. Sci. 61, 23–84.

Schleicher, H., Wiedemann, G., Wöhl, H., Berkefeld, T., Soltau, D., 2004. Detection of neutral sodium above Mercury during the transit on 2003 May 7. Astron. Astrophys. 425, 1119–1124.

Shemansky, D.E., 1988. Revised atomic species abundances at Mercury: the debacle of bad g values. Mercury Messenger 2 (August).

Shemansky, D.E., 2003. The role of solar wind heavy ions in the space environment. In: Rarefied Gas Dynamics: 23rd International Symposium. AIP Conference Proceedings, vol. 663, pp. 687–695, doi:10.1063/1.1581610.

Sigmund, P., 1969. Theory of sputtering. I. Sputtering yield of amorphous and polycrystalline targets. Phys. Rev. 184, 383–416.

Siscoe, G., Christopher, L., 1975. Variations in the solar wind stand-off distance at Mercury. Geophys. Res. Lett. 2, 158–160.

Slavin, J.A., Holzer, R.E., 1979. The effect of erosion on the solar wind stand-off distance at Mercury. J. Geophys. Res. 84, 2076–2082.

Smyth, W.H., Marconi, M.L., 1995. Theoretical overview and modeling of the sodium and potassium atmospheres of Mercury. Astrophys. J. 441, 839–864.

Sprague, A.L., Kozlowski, R.W.H., Hunten, D.M., 1993. An upper limit on neutral calcium in Mercury's atmosphere. Icarus 104, 33–37.

Sprague, A.L., Kozlowski, R.W.H., Witteborn, F.C., Cruikshank, D.P., Wooden, D.H., 1994. Mercury: mid-infrared (7.3–13.5 μm). Spectroscopic observations showing features characteristic of plagioclase. Icarus 109, 156–167.

Sprague, A.L., Hunten, D.M., Lodders, K., 1995. Sulfur at Mercury, elemental at the poles and sulfides in the regolith. Icarus 118, 211–215.

Sprague, A.L., Kozlowski, R.W.H., Hunten, D.M., Schneider, N.M., Domingue, D.L., Wells, W.K., Schmitt, W., Fink, U., 1997. Distribution and abundance of sodium in Mercury's atmosphere, 1985–1988. Icarus 129, 506–527.

Sprague, A., Emery, J.P., Donaldson, K.L., Russel, R.W., Lynch, D.K., Mazuk, A.L., 2002. Mercury: mid-infrared (3–13.5 μm) observations show heterogeneous composition, presence of intermediate and basic soil types, and pyroxene. Meteor Plan. Sci. 37, 1255–1268.

Sprague, A., Warell, J., Cremonese, G., Langevin, Y., Helbert, J., Wurz, P., Veselovsky, I., Orsini, S., Milillo, A., 2007. Mercury's surface composition and character as measured by ground-based observations. Space Sci. Rev. 132, 399–431.

Sprague, A.L., Donaldson Hanna, K.L., Kozlowski, R.W.H., Helbert, J., Maturilli, A., Warell, J.B., Hora, J.L., 2009. Spectral emissivity measurements of Mercuy's surface indicate Mg- and Ca-rich mineralogy, K-spar, Na-rich plagioclase, rutile, with possible perovskite, and garnet. Planet. Space Sci. 57, 364–38331.

Thomas, C.W., Aitchison, J., 2006. Log-ratios and geochemical discrimination of Scottish Dalradian limestones: a case study. Compositional Data Analysis in the Geosciences: from Theory to Practice, Geological Society, London, Special Publications, vol. 264, pp. 25–41.

Thompson, M.W., Farmery, B.W., Newson, P.A., 1968. A mechanical spectrometer for analysing the energy distribution of sputtered atoms of copper and gold. Philos. Mag. 18 (152), 361–383.

Warell, J., 2003. Properties of the Hermean regolith: III. Disk-resolved vis-NIR reflectance spectra and implications for the abundance of iron. Icarus 161, 199–222.

Warell, J., Blewett, D.T., 2004. Properties of the Hermean regolith: V. New optical reflectance spectra comparison with lunar anorthosites, and mineralogical modelling. Icarus 168, 257–276.

Warell, J., Sprague, A.L., Emery, J.P., Kozlowski, R.W.H., Long, A., 2006. The 0.7–5.3 μm IR spectra of Mercury and the Moon: evidence for high clinopyroxene on Mercury. Icarus 180, 281–291.

Westley, M.S., Baragiola, R.A., Johnson, R.E., Baratta, G.A., 1995. Ultraviolet photodesorption from water ice. Planet. Space Sci. 43 (10/11), 1311–1315.

Wood, J.A., Buck, W.R., Anders, E., Morgan, J.W., Stolper, E., Anderson, D.L., Kaula, W.M., Consolmagno, G.J., Ringwood, A.E., Wänke, H., 1981. Geophysical and cosmophysical constraints on the properties of mantles of the terrestrial planets. Basaltic Volcanism on the Terrestrial Planets. Pergamon Press, pp. 633–699.

Wurz, P., Lammer, H., 2003. Monte-Carlo simulation of Mercury's exosphere. Icarus 164 (1), 1–13.

Wurz, P., Wimmer-Schweingruber, R., Bochsler, P., Galvin, A., Paquette, J.A., Ipavich, F., 2003. Composition of magnetic cloud plasmas during 1997 and 1998. Solar Wind X. American Institute Physics, 679, 685–690.

Wurz, P., 2005. Solar wind composition. The Dynamic Sun: Challenges for Theory and Observations, ESA SP-600, pp. 1–9.

Wurz, P., Rohner, U., Whitby, J.A., Kolb, C., Lammer, H., Dobnikar, P., Martín-Fernández, J.A., 2007. The Lunar exosphere: the sputtering contribution. Icarus 191, 486–496. doi:10.1016/j.icarus.2007.04.034.

Yakshinskiy, B.V., Madey, T.E., 1999. Photon-stimulated desorption as a substantial source of sodium in the lunar atmosphere. Nature 400, 642–644.

Yakshinskiy, B.V., Madey, T.E., Ageev, V.N., 2000. Thermal desorption of sodium atoms from thin SiO_2 films. Surf. Sci. Lett. 7, 75–87.

Ziegler, J.F., 2004. SRIM-2003. Nucl. Instrum. Methods B 219, 1027–1036.

Ziegler, J.F., Biersack, J.P, Littmark, U., 1984. The Stopping and Range of Ions in Solids, vol. 1 of series Stopping and Ranges of Ions in Matter. Pergamon Press, New York.

Zurbuchen, T.H., Raines, J.M., Gloeckler, G., Krimigis, S.M., Slavin, J.A., Koehn, P.L., Killen, R.M., Sprague, A.L., McNutt Jr., R.L., Solomon, S.C., 2008. MESSENGER observations of the composition of Mercury's ionized exosphere and plasma environment. Science 321, 90. doi:10.1126/science.1159314.

Corrigendum

Corrigendum to "Self-consistent modelling of Mercury's exosphere by sputtering, micrometeorite impact and photon-stimulated desorption" [Planet. Space Sci. 58 (2010) 1599–1616]

P. Wurz [a],*, J.A. Whitby [a,1], U. Rohner [a,2], J.A. Martín-Fernández [b], H. Lammer [c], C. Kolb [c,3]

[a] Physikalisches Institut, Universität Bern, Sidlerstrasse 5, CH-3012 Bern, Switzerland
[b] Department for Computer Science and Applied Mathematics, University of Girona, Edifici P-IV, Campus Montilivi, E-17071 Girona, Spain
[c] Space Research Institute, Austrian Academy of Sciences, Schmiedlstrasse 6, A-8042 Graz, Austria

Authors regret that captions were not included in published paper. Captions are as follows:

Fig. 1. Schematic representation of the derivation of the mineralogical composition of Mercury's surface, using observational constraints and modelling.

Fig. 2. Normalised energy distribution for sputtered H, O, Ca, and Fe atoms according to Wurz et al. (2007) using incident protons of 1 keV energy. The vertical lines indicate the escape energy for these atoms above which an atom will escape from Mercury's exosphere.

Fig. 3. Top panels: density profiles of atoms sputtered from Mercury's surface for a solar wind velocity of $v_{SW}=440$ km/s, a flux hitting the surface of $f_{SW}=4.10\times10^{12}$ m^{-2} s^{-1}, composed of 95% protons and 5% alpha particles. Bottom panels: density profiles of atoms released by MIV from Mercury's surface. The two surface compositions are given in Table 2. The kinks and noise in the curves at low densities are an artefact of the Monte Carlo simulation because of the finite number of particles in the simulation.